REPORT DOCUMENTATION PAGE

AFRL-SR-BL-TR-00-

0824

1. AGENCY USE ONLY *(Leave blank)*	2. REPORT DATE	3.
	18 Dec 00	Final Report: 02 Oct 97 - 11 Sep 99

4. TITLE AND SUBTITLE

Investigation of the Laser Material Interaction Regimes During Thermal and Compositional Superposition in Laser Surface Improvement

5. FUNDING NUMBERS

F49620-97-1-0121

6. AUTHOR(S)

Dr. Mary Helen McCay
Dr. John Hopkins

7. PERFORMING ORGANIZATION NAME(S) AND ADDRESS(ES)

University Of Tennessee/Space Institute
411 B. H. Goethert Parkway
Tulahoma, TN 37388-8897

8. PERFORMING ORGANIZATION REPORT NUMBER

9. SPONSORING/MONITORING AGENCY NAME(S) AND ADDRESS(ES)

AFOSR
801 N. Randolph St. Suite 732
Arlington VA 22203

10. SPONSORING/MONITORING AGENCY REPORT NUMBER

11. SUPPLEMENTARY NOTES

12a. DISTRIBUTION AVAILABILITY STATEMENT

Approved for public: Distribution unlimited

12b. DISTRIBUTION CODE

13. ABSTRACT *(Maximum 200 words)*

The objectives of the research are to 1) understand the reactions occurring within the indexed and surrounding regions as a result of the thermal and compositional cycling experienced during the formation of a laser surface modified layer, and 2) to evaluate the process kinetics, solidification and growth morphologies based on thermodynamic and heat conduction considerations. In order to accomplish these objectives, the laser surfacing process was divided into three significant categories. These are 1) the alloyed surface region and the phase reactions within that surface, 2) the grain growth/solid state transformation and tempered regions and the transformations within those regions, and 3) the thermal temporal history occurring during processing as determined both experimentally and computationally. Processing parameters for all of the trials are given in Table I. Compositions of the base alloys used are given in Table II. In all cases, a Nd:YAG fiber optically delivered laser was used.

20001227 078

14. SUBJECT TERMS

Investigation of the laser material interaction regimes during thermal and compositional superposition in laser surface improvement

15. NUMBER OF PAGES

37

16. PRICE CODE

17. SECURITY CLASSIFICATION OF REPORT	18. SECURITY CLASSIFICATION OF THIS PAGE	19. SECURITY CLASSIFICATION OF ABSTRACT	20. LIMITATION OF ABSTRACT
UNCLASSIFIED	UNCLASSIFIED	UNCLASSIFIED	UU

AIR FORCE OFFICE OF SCIENTIFIC RESEARCH

FINAL REPORT

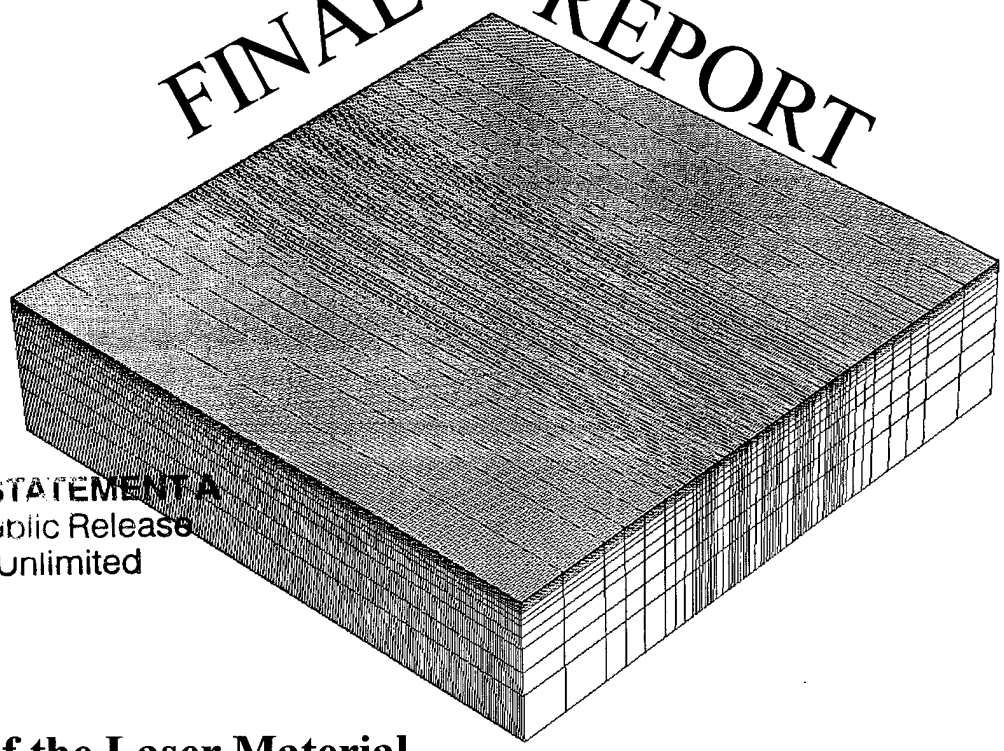

Investigation of the Laser Material Interaction Regimes During Thermal and Compositional Superposition in Laser Surface Improvement

The University of Tennessee Space Institute
Center for Laser Applications
Accomplished Center of Excellence
Tullahoma, Tennessee 37388

AFOSR FINAL REPORT

Investigation of the Laser Material Interaction Regimes During Thermal and Compositional Superposition In Laser Surface Improvement

BACKGROUND

During Laser Surface Alloying (LSA), additives are applied to a base material in such a way that upon melting a thin region of the surface, significant alloying between the additive and the base material occurs. This is demonstrated in Figure 1 which is a schematic of a LISI[SM] (Laser Induced Surface Improvement) surface. In this case, the additive is applied with a surface slurry prior to melting. The laser beam is then passed across the surface, alloying the additive into the substrate. To cover large surfaces, the laser beam is indexed in sequential overlaps. The goal of LSA is to obtain properties that both differ from the substrate, and provide some form of desired protection (wear, corrosion, etc.). This enables the user/designer to select a base material for its desirable properties without having to compromise those properties in order to survive a harsh environment.

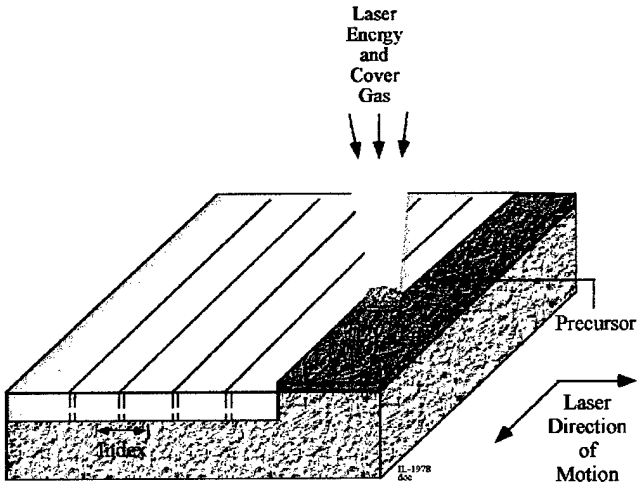

Figure 1. Schematic of LISI Process.

Since LSA involves the spatial and temporal input of heat into the base material in order to affect the alloying, both the alloying process itself and the influence of the heat upon the surface and base material must be considered. A schematic for a typical material is seen in Figure 2 and shows that in addition to the surface alloying and depending upon the type of base material (steel, aluminum alloy, etc.), numerous metallurgical events can occur beneath the alloyed region. Add to this the additional complexity of indexing or overlapping successive beams to create large surfaces, and the challenge of understanding the LSA process grows to tremendous proportions. This research seeks to address some aspects of that challenge.

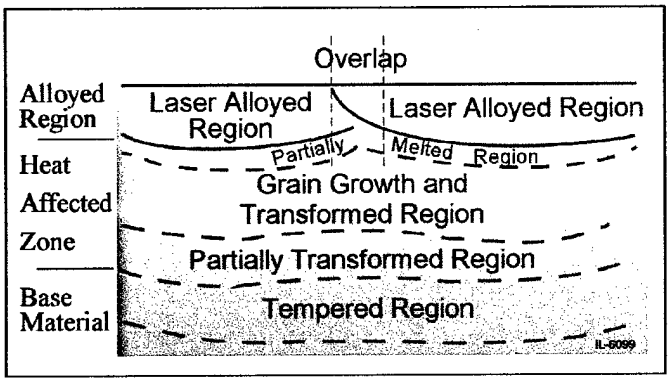

Figure 2. A schematic of the regions that occur in a material during laser surface.

OBJECTIVES

The objectives of the research are to 1) understand the reactions occurring within the indexed and surrounding regions as a result of the thermal and compositional cycling experienced during the formation of a laser surface modified layer, and 2) to evaluate the process kinetics, solidification and growth morphologies based on thermodynamic and heat-conduction considerations. In order to accomplish these objectives, the laser surfacing process was divided into three significant categories. These are 1) the alloyed surface region and the phase reactions within that surface, 2) the grain growth/solid state transformation and tempered regions and the transformations within those regions, and 3) the thermal temporal history occurring during processing as determined both experimentally and computationally.

Processing parameters for all of the trials are given in Table I. Compositions of the base alloys used are given in Table II. In all cases, a Nd:YAG fiber optically delivered laser was used.

TABLE I
Processing Conditions

CHROMIUM ADDITIONS

Power (watts)	Speed (mm/sec)	Index (mm)	Beam Size (mm)
1500	4500	0.25	1.0
		0.50	
		0.75	
		1.0	

CHROMIUM, NICKEL, WC AND SiC ADDITIONS

Power (watts)	Speed (mm/sec)	Index (mm)	Beam Size (mm)
2000	1000	2.5	0.75 x 4
	1500		
	2250		
	3000		

CHROMIUM AND CrB_2 ADDITIONS

Power (watts)	Speed (mm/sec)	Index (mm)	Beam Size (mm)
1500	2000	3.5	0.75 x 4
	1500		

TABLE I Cont.

4340 PROCESSING

Power (watts)	Speed (mm/sec)	Index (mm)	Beam Size (mm)
500	1000	1.5.2.5	1 x 3
	1250	1.5.2.5	
	1500	1.5.2.5	
	1750	1.5.2.5	
	2000	1.5.2.5	
	2250	1.5.2.5	
	2500	1.5.2.5	
	3000	1.5.2.5	
	3500	1.5.2.5	
	4000	1.5.2.5	
	4500	1.5.2.5	

IL-6096

HEAT TREATED 4340 PROCESSING

Power (watts)	Speed (mm/sec)	Index (mm)	Beam Size (mm)
500	500	N/A	0.75 x 3
750	1000		
1000	2000		
1500			

THERMAL PROCESSING TRIALS

Beam Translation Velocity (mm/min)	Beam Index (mm)	Beam Size (mm)
1000	1.5, 2.5	1 x 3
1250	1.5, 2.5	
1500	1.5, 2.5	
1750	1.5, 2.5	
2000	1.5, 2.5	
2250	1.5, 2.5	
2500	1.5, 2.5	
3000	1.5, 2.5	
3500	1.5, 2.5	
4000	1.5, 2.5	
4500	1.5, 2.5	

IL-6096

TABLE II

Set	Speed (mm/min)	Layer Depth (μm)	Average Hardness (Knoops)	Average Composition (rem Fe)				Total Carbides (wt%)	Carbide/Iron/Silcon Phase (1►4)
				Cr wt%	Ni wt%	Si(C) wt%	W(C) wt%		
A	1000	462	576 ± 64	10.2	2.0	7.5	4.2	11.7	(Least) 1
B	1500	315	634 ± 59	12.4	2.0	8.7	5.2	13.9	2
C	2250	231	644 ± 97	13.3	2.0	9.1	6.3	15.4	3
D	3000	246	741 ± 161	17.9	2.0	12.2	8.4	20.6	(Most) 4
E (4340P)	1500		590	0.8	1.8	0	0	0	
F (4340)			270						IL-6096

I. The Alloyed Surface Region

A systematic approach was adopted to investigating the alloyed surface region in steels. This began with the addition of one element, chromium, and continued with additions of nickel, WC and SiC, and then CrB_2.

Chromium Additions

A series of sequential laser surface modification experiments was completed with the associated compositional, microstructural and mechanical property determinations. This involved a matrix of samples which were processed on 1010 steel with chromium additive since there is a large amount of information on iron/chromium alloys. The resultant alloyed regions ranged in depth from 100 microns to 500 microns and with total widths up to 60 mm. Selected track sequences on each sample were submitted to examination at ten micron intervals to produce maps of composition, phase and microhardness. The compositions matched those calculated using a precursor density of 80%. The phases were predictable by using the Schaeffler diagram [1]. This indicates that for LSA using single, non-complex elements, predictions of composition and phase are straight forward.

Surface roughness variation was dependant on processing energy while the layer depth and volume for each alloy was found to be dependent not only on input power and energy but on the indexing. As the index increased (i.e., the distance between successive passes increased), the depth and volume increased. This is due to the fact that when the laser is indexed, it strikes both already-processed surface and new surface slurry. Since an increase in index assures that there will be a larger area of fresh slurry, the absorptivity to the Nd:YAG laser beam is being assisted by the presence of the slurry. Other possible contributors, such as changes in conductivity or fluidity due to the chromium additions, can be eliminated since there is no indexing effect on the amount of chromium dissolved per volume.

Layer hardness was also found to be related to indexing as well as input power. This is illustrated in Figure 3 which shows the region of maximum hardness in the heat affected zone in the low energy (23.33 joules/mm^2) sample while the higher energy (93.3 joules/mm^2) sample has maximum hardness within the layer itself. This effect is felt to reflect the strong influence of repetitive temperature passes on both the alloyed region and the HAZ and emphasizes the necessity for further study of the superposition of overlapping tracks.

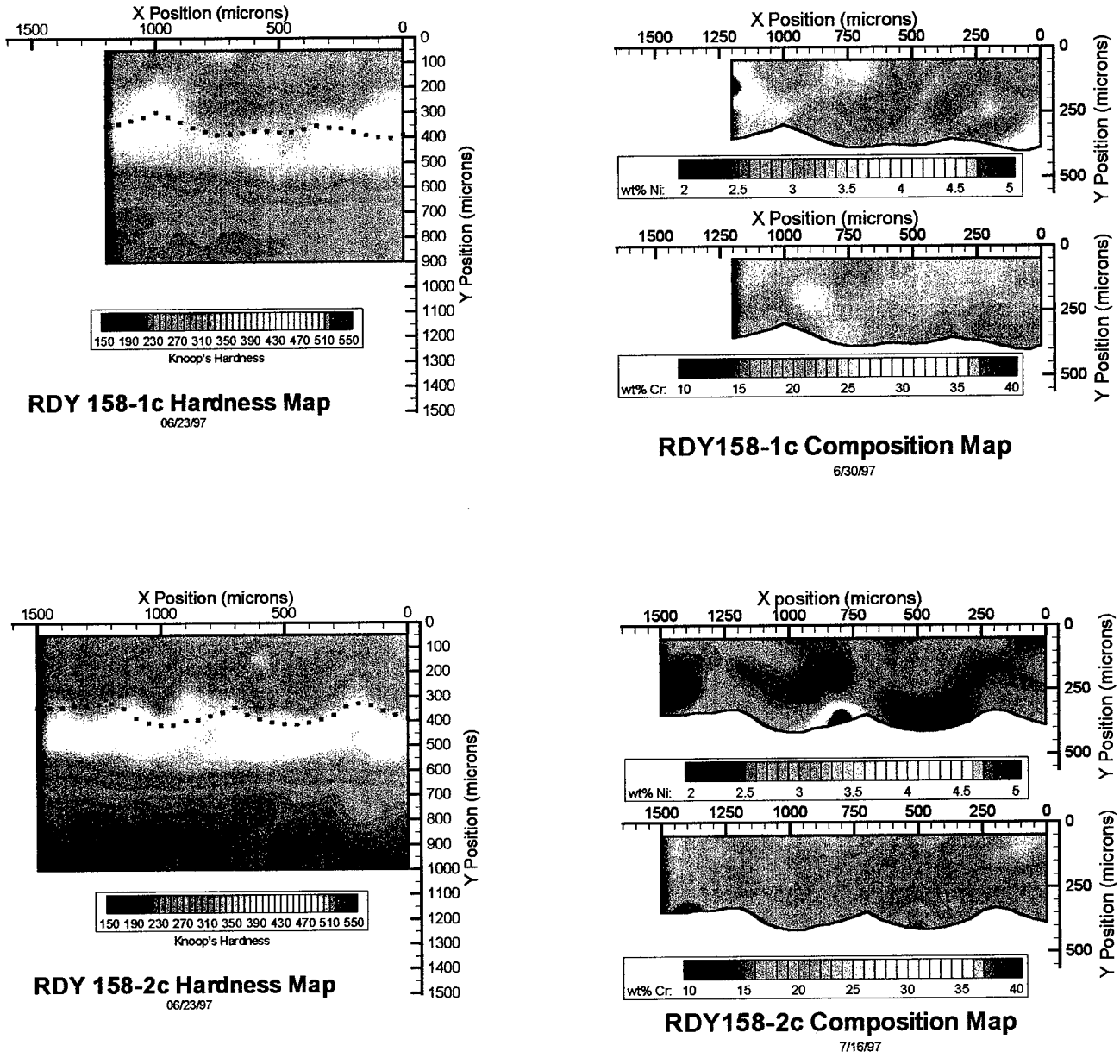

Figure 3.

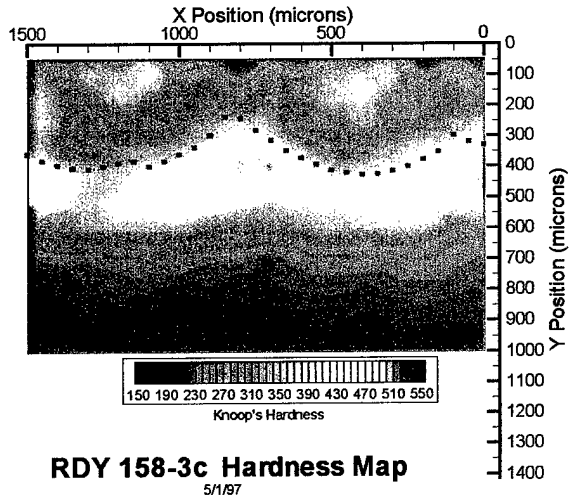

RDY 158-3c Hardness Map
5/1/97

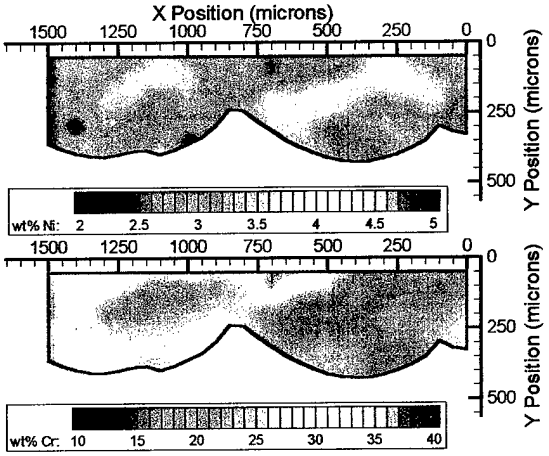

RDY158-3c Composition Map
6/30/97

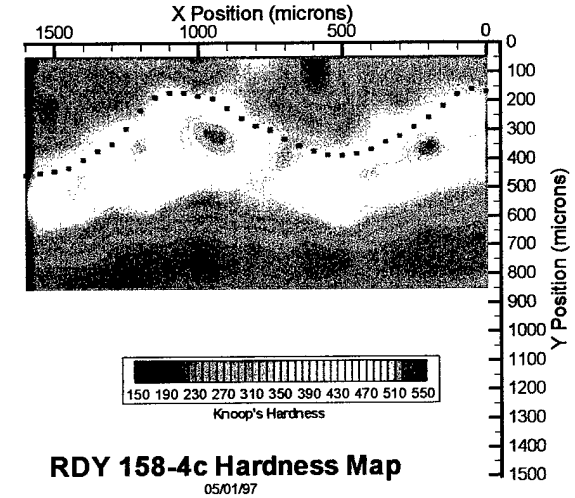

RDY 158-4c Hardness Map
05/01/97

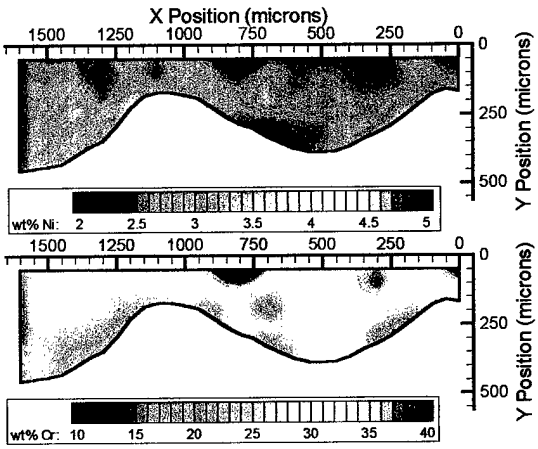

RDY158-4c Composition Map
6/30/97

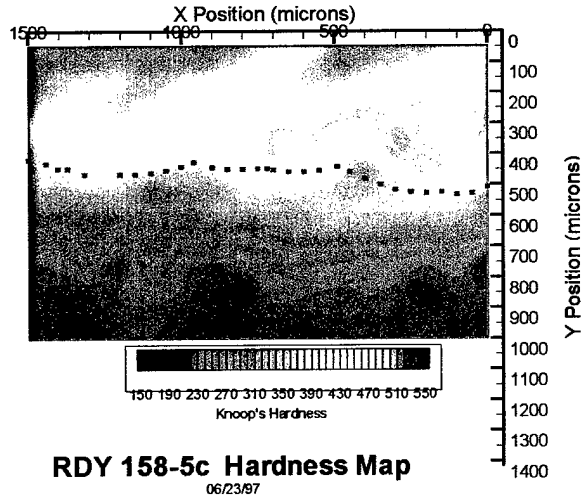

RDY 158-5c Hardness Map
06/23/97

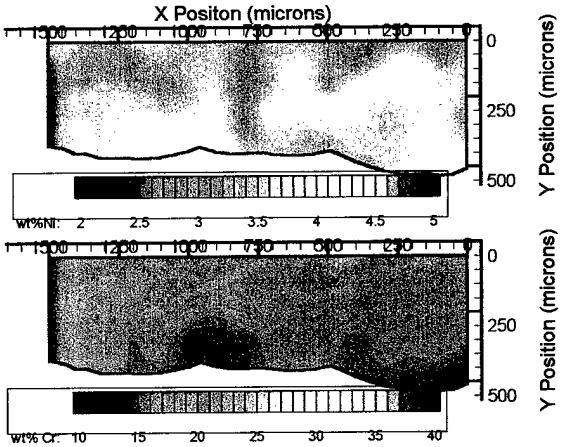

RDY158-5c Composition Map
7/01/97

Figure 3. Continued.

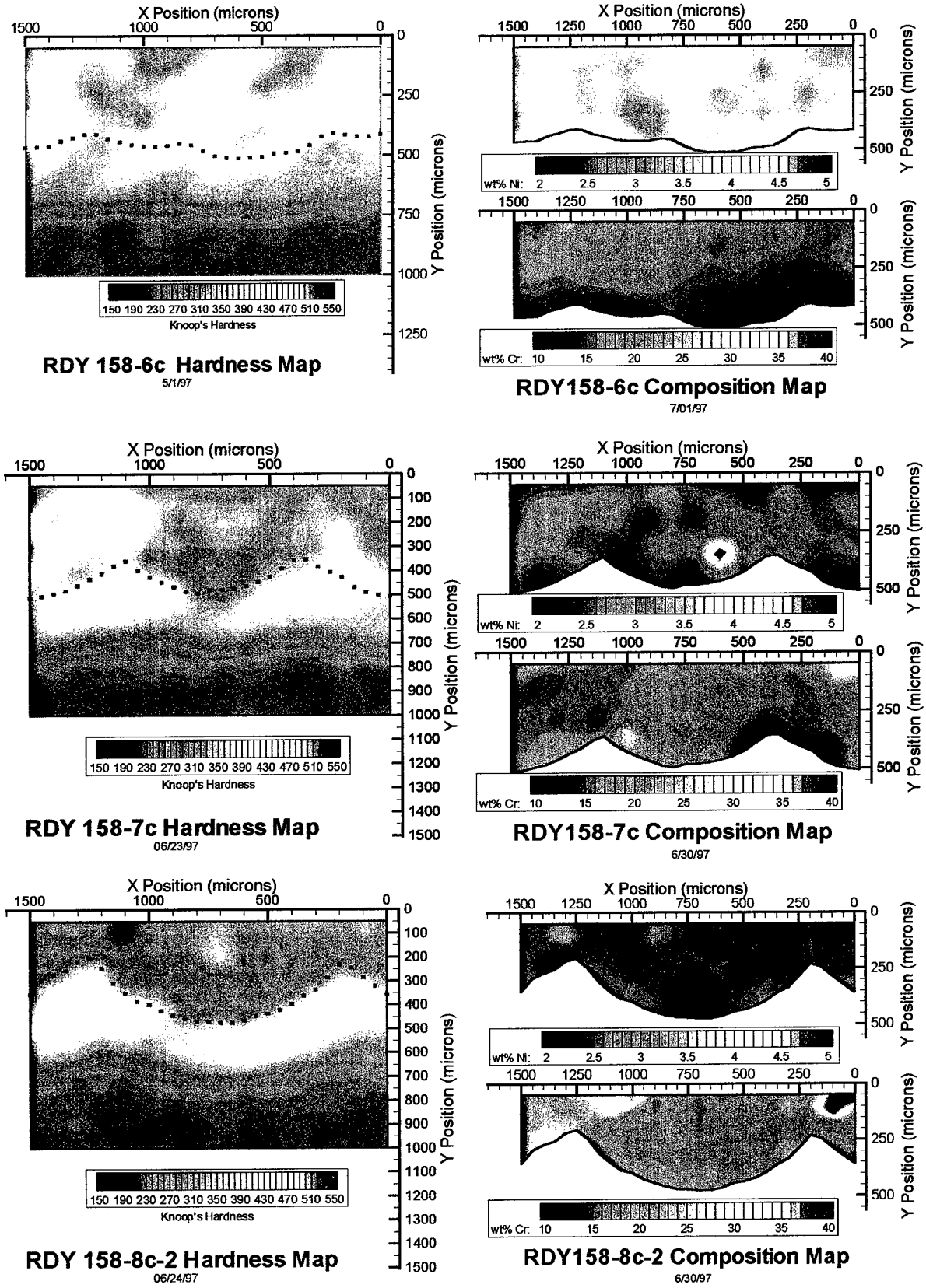

Figure 3. Continued.

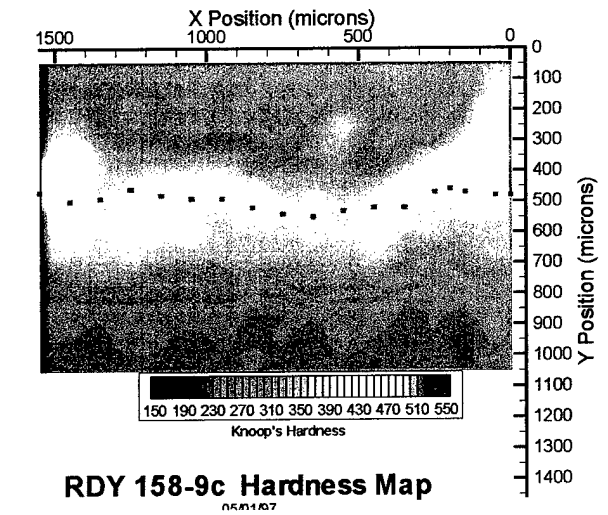

RDY 158-9c Hardness Map

05/01/97

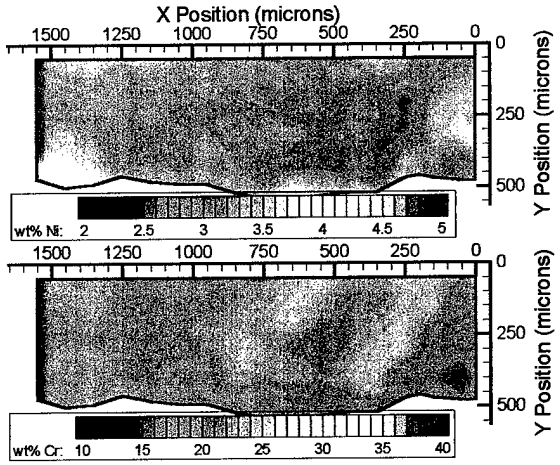

RDY158-9c Composition Map

7/01/97

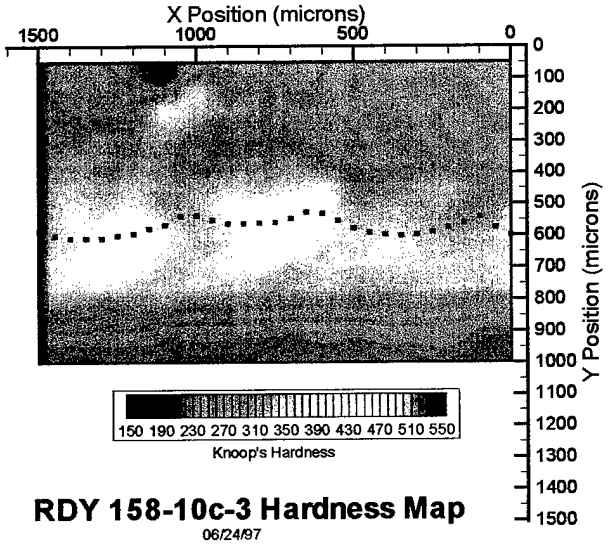

RDY 158-10c-3 Hardness Map

06/24/97

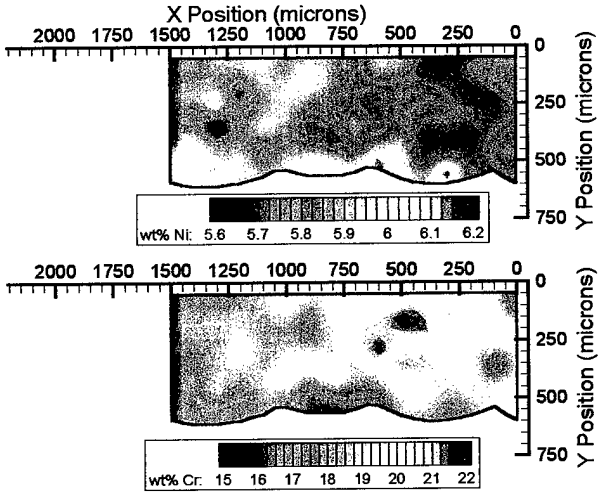

RDY158-10c-3 Composition Map

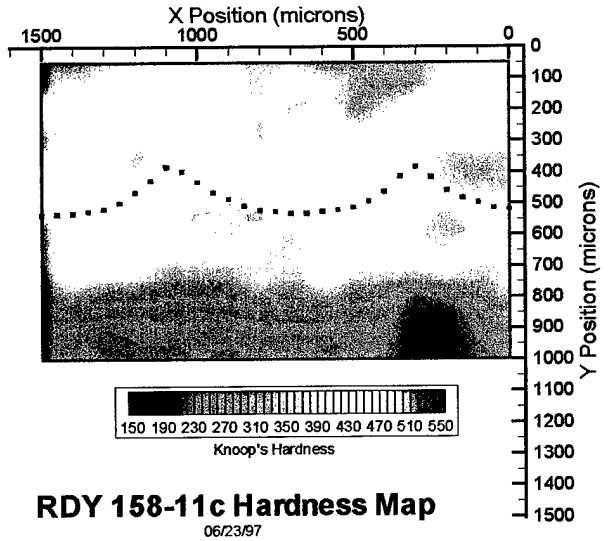

RDY 158-11c Hardness Map

06/23/97

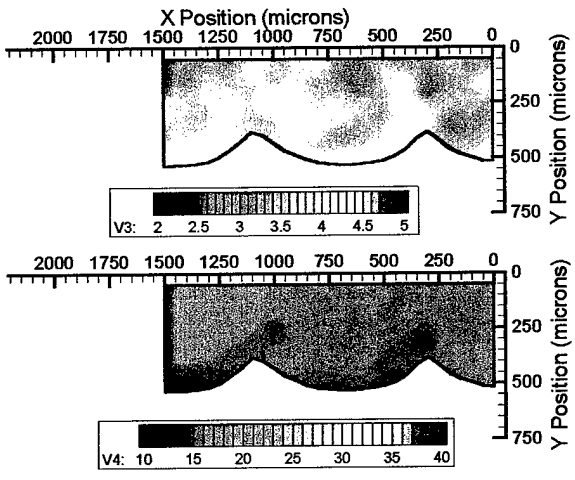

RDY158-11c Composition Map

9/30/97

Figure 3. Continued.

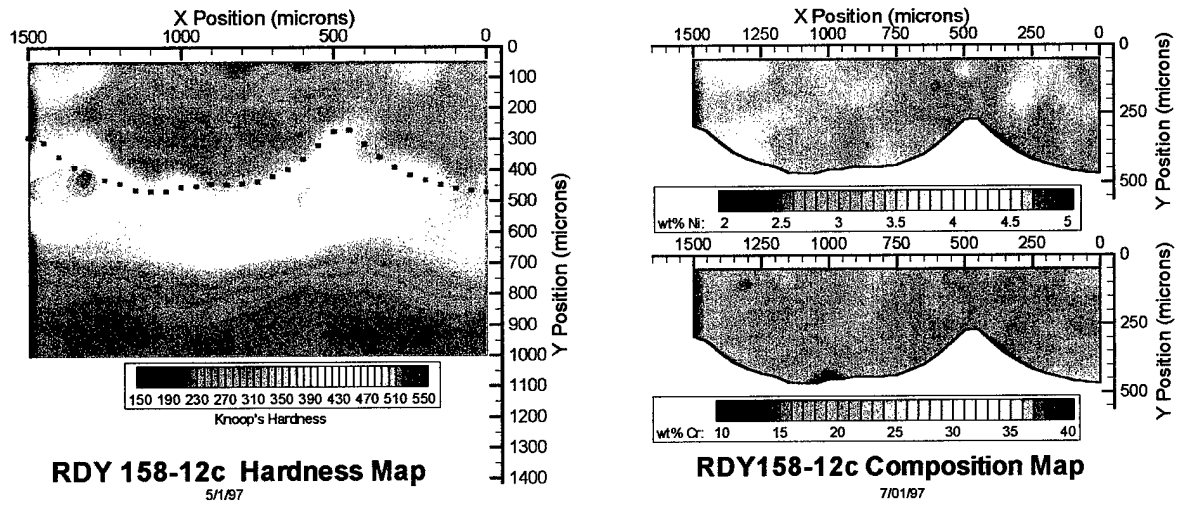

Figure 3. Cont.

Chromium, Nickel, WC and SiC Additions

Further additions were made to the surface slurry in order to alter the composition and therefore phase transformations. The addition of the elements chromium and nickel enhance the corrosion resistance, particularly when chromium exceeds 12 wt%, making them desirable additions to the surface of a steel material. They also dictate predictable phase changes, with chromium being a ferrite former and nickel an austenite former, therefore, reducing the hardening due to martensitic transformation. The phases present should be predictable from the Schaeffler diagram using compositional analysis of the layers and the overall hardness can then be predicted using weighted hardness values for the individual phases. These phase alterations can produce a significant secondary effect in the surface alloy by reversing the residual stresses from the compressive stresses expected in a martensitic surface to the tensile stresses in an austenite surface [2, 3]. Corrosion protection can be obtained while producing a variety of steel phases by varying the composition with the processing parameters.

Carbides on the other hand increase the hardness and wear resistance, but their chemistry must be considered during processing since their decomposition can alter the steel phases by supplying either carbon, which is an austenite former, the individual elements of tungsten and silicon, which are ferrite formers, or new carbides. The dissociation of the carbide additives is a strong possibility during laser processing with its intense energy density. For example, although WC is chemically stable rather stable, it decomposes into its components above 2600°C [4], a temperature well within the regime of laser surface processing. Therefore the WC and SiC were added to determine if the surface alloy properties could be predicted using the Schaeffler diagram and hardness values for the phases and carbides.

Steel coupons of 4340 steel (6 x 76 x 154 mm) were used as substrates for these experiments. The 4340 was selected because it is generally the standard to which other high strength steels are compared and combines hardenability with ductility, toughness and strength.

In addition, it has good strength at elevated temperatures and is readily heat-treatable. The large surfaces of the substrates were sandblasted and then coated with a slurry comprised of chromium (44 wt%), nickel (22 wt%), silicon carbide (3 wt%) and tungsten carbide (8 wt%) powder, varnish and mineral spirits. Once the slurry had dried at room temperature, processing proceeded For baseline purposes, an uncoated sample of 4340 was processed.

Subsequent to processing, the sample surfaces were examined optically for signs of cracking. Each was then cut into pieces for more extensive analysis. Energy dispersive spectroscopy (EDS) (standardless, background removed) analysis was used for determination of the chromium, nickel, silicon and tungsten content. Using a second set of samples, further analysis was conducted by x-ray diffraction (CuKα, 1.54 A° wavelength radiation), first on the as-processed surface, then on the same with 100 microns of the surface removed. Wear properties of were ascertained by two sets of wear testing (block-on-disc apparatus at 1000 rpm (280 mm/min) and 4 lbs. Normal weight) to determine weight loss/minute and friction coefficient after 2, 10 and 20 minutes.

A compilation of the characterization results is given in Tables II and III (average values). The samples (A, B, C, and D) are presented in order of increased processing speed. Comparison data for 4340 processed (E) and as received (F) is also given. All of the sample surfaces exhibited some evidence of surface micro-cracking (Figure 4) indicative of residual stresses. From Table II it can be seen that the chromium and carbide contents vary inversely to the depth of the layers. The nickel content however, remains at 2%, which is around the limit of accuracy of the analysis technique. The cracking increased in severity from Set A to D (Table III), with D containing the highest amount of inclusion induced fracture sites. Set A had relatively little cracking which occurred primarily at the midpoint of the beam track. Sets C and D had extensive cracking exhibiting extremely brittle failure and penetrating the depth of the processed region. Using calculations of the chromium and nickel equivalents and a calculated value of the amount of carbon present (assuming dilution from alloying), the percentage of the martensite, austenite and ferrite phases in each sample were estimated from the Schaeffler diagram and are given in Table III. This was contrary to what was

TABLE III

Set	Cracking Severity (1 - 4)	Crack Location	Predicted Schaeffler Phases			Observed Phases
			Martensite vol%	Ferrite vol%	Austenite vol%	
A	(Least) 1	Overlap	91	0	9	Austenite/ferrite
B	2	Mid track	68	0	32	Austenite/ferrite
C	3	Both	60	0	40	Austenite/ferrite
D	(Most) 4	Both/chunks	10	4	86	Austenite/ferrite
E			100	0	0	Martensite/ferrite
F						

IL-6096

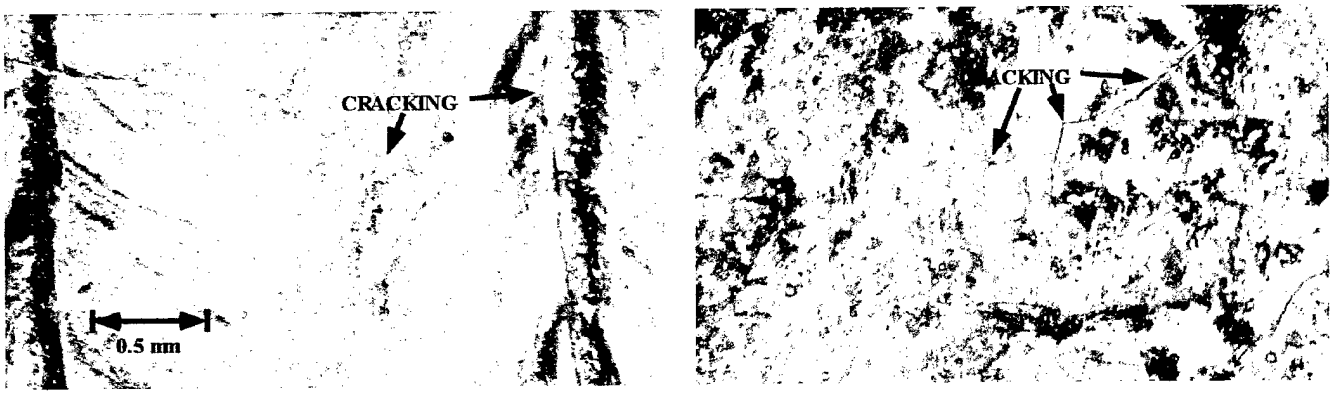

Figure 4. Surface cracking after processing at 2000 W and (a) 1000 mm/min, sample A and (b) 2250 mm/min, sample C.

observed from the x-ray diffraction analysis which showed that A contained significant austenite indicating a shift toward higher carbon, while the remaining samples had noticeable ferrite content. Thus the predictions using the Schaeffler diagram should be shifted toward higher chromium equivalents and therefore more ferrite. This is probably due to the dissociation of the carbides since indications from the x-ray of any remaining undissociated SiC and WC were very weak, although sample D evidenced a large amount of SiC-5H. In addition, when the surfaces were removed, the remaining layers all strongly indicated the presence of a carbon-iron-silicon (12, 79, 9 wt%) phase suggesting a dissociation of the incorporated silicon carbide and a non-stoichiometric composition of Si-C compound. The degree of occurrence of this newly formed carbide is given in Table II and indicates the possibility that some elemental silicon, which is a ferrite former, was present in the alloyed layer. Interestingly, the occurrence of the C-Fe-Si phase increases as the interaction time (inverse to speed of processing) decreased, suggesting a non-equilibrium phase.

As can be seen in Table III, the average microhardness varies inversely with layer depth. The standard deviation is also given, so an appreciation can be gained for the extent of inhomogeneity within the sets, which is also reflected in the microhardness maps shown in Figure 5 (the light regions indicate high hardness). A plot of average microhardness vs. the total silicon plus tungsten percent (Figure 6) reveals a linear relationship which when curve-fit yields the following:

$$\text{Microhardness} = 373 + 17.9\ (\text{wt\% carbides})$$

Using this relationship between hardness and weight percent silicon plus tungsten, the hardness of the silicon plus tungsten additives can be calculated to be 2100 Knoops, an acceptable value for carbides based on the literature [5]. The matrix material however (zero wt% Si+W) has a Knoops hardness significantly lower than the hardness of sample E, the processed

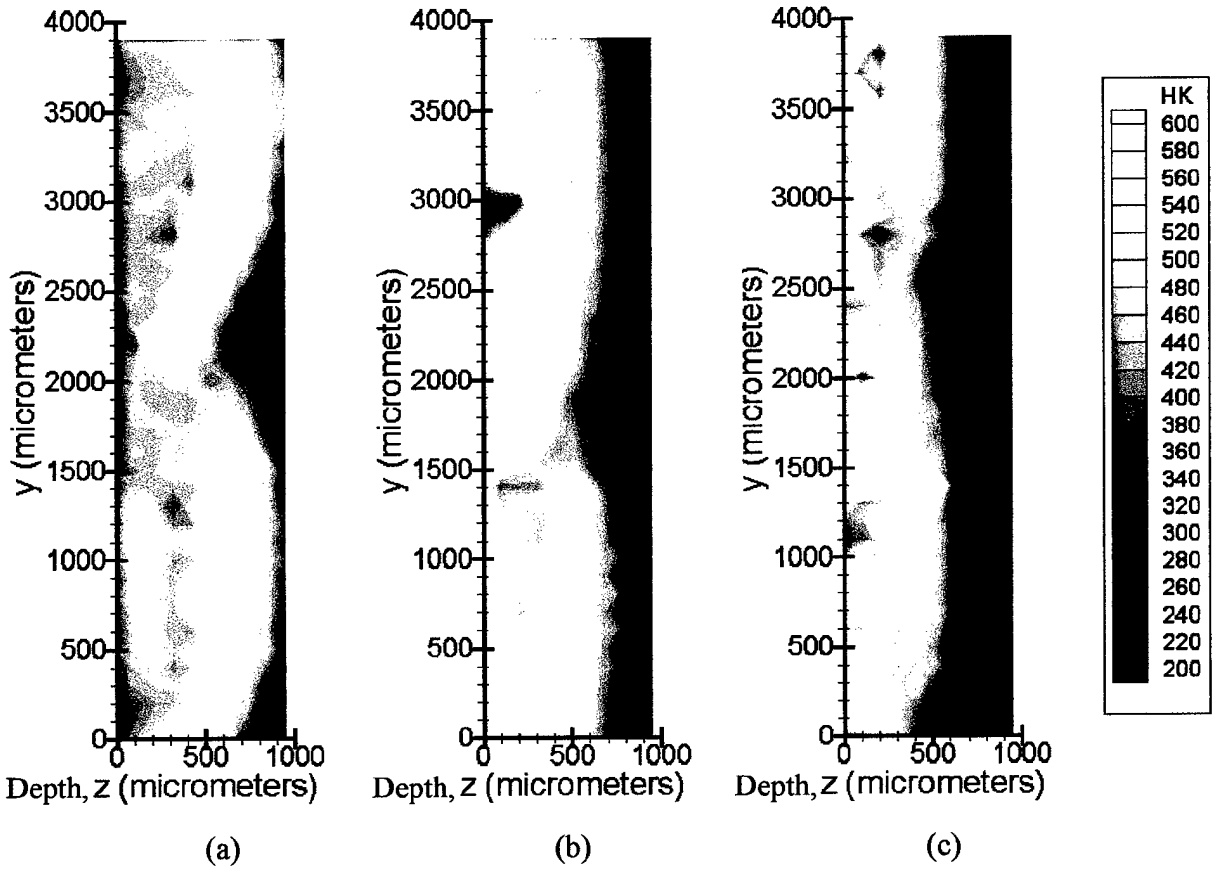

Figure 5. Microhardness maps of samples (a) A, (b) B, and (c) C, showing the cross-section depth perpendicular to the surface, (z =ϕ is the surface).

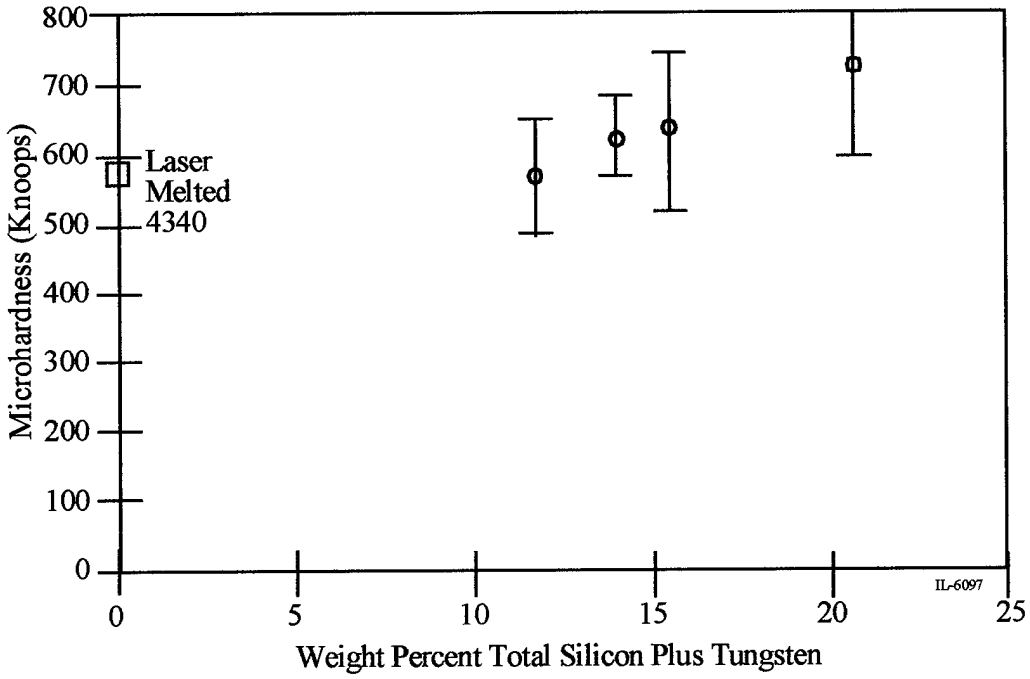

Figure 6. Plot of average Knoops microhardness vs. silicon plus tungsten weight percent.

matrix material with no alloying addition. Sample E's value of 590 Knoops is in keeping with predictions for transformed 4340 with approximately 100% martensite. This suggests that the microhardness of the resolidified matrix is also being affected by the alloying additions and the formation of the new C-Fe-Si phase and that the hardness of the layer is dominated by the addition of the carbides.

Wear test results are given in Figure 7, which gives grams lost per minute over a ten minute period for the base 4340(F) as well as the processed 4340(E) and the sample surfaces. In two of the samples (A and D), the addition of chromium, nickel and the carbides increased the wear over the processed and unprocessed base material. In samples B and C, the wear was slightly or similar to the base. High wear would be expected in the softer sample A, and high wear would also be expected in the harder sample D which was seen to exhibit significant cracking and loss of chunks of material during testing. This is not expected either from the Schaeffler predictions or the observed phases and therefore substantiates the conclusion that there are significant (and sometimes unknown) phase variations during laser surface processing when a variety of additives are employed.

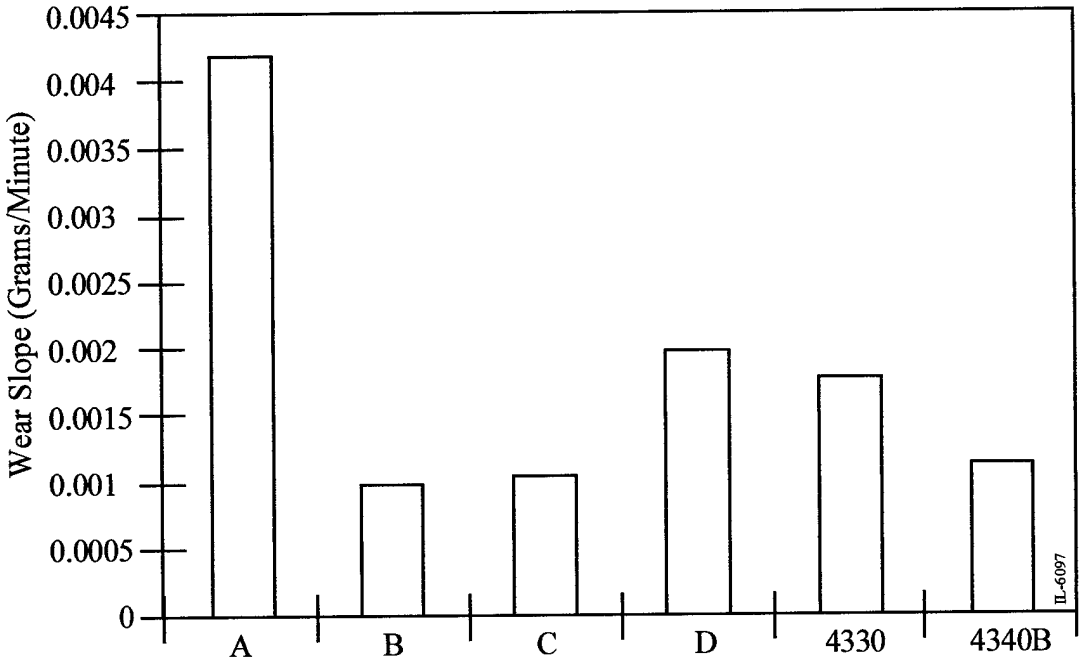

Figure 7. Wear slopes of processed and unprocessed 4340 samples (block-on-disc apparatus at 280 m/min and 4 lbs normal weight).

Chromium and CrB_2 Additions

Heat treated 4340 (450 Knoops) was also used for these experiments. Ten micron size Cr and CrB2 powders were mixed in ratios from 10Cr/90CrB_2 to 90Cr/10CrB_2 in increments of ten. These mixtures were then dispersed in a slurry, sprayed onto the steel surface to a thickness of 100 microns and processed. The samples were sectioned for compositional analysis, microhardness, surface roughness, wear testing (block-on-disc at 280 mm/min), abrasion testing (50 – 70 grit A.F.S. testing sand at 2000 revolution increments, wheel diameter 8 inches) and x-ray diffractometry (CuK_a radiation). Corrosion properties were ascertained by corrosion testing in a Q-Fog chamber (ptt 6.5-7.2, 5 wt% NaCl, 35°C, 100% relative humidity) for 24 hours.

Data from some of the analyses are shown in Table IV. Figures 8 through 10 show the results of the microhardness, wear and abrasion tests as a function of the percent of CrB_2 in the slurry. The microhardness increases linearly with increasing CrB_2 until reaching the highest percentage sample. A linear regression curve-fit of the data gives an average slope of 16 Knoops per wt% CrB_2 and an intercept of 167 Knoops. The low intercept value indicates that the matrix is significantly softer than quenched 4340 steel and probably represents the steel alloyed with chromium to produce softer ferrite. The effect of the hardness increase can be seen in the wear test results, which show a related decrease in wear as the CrB_2 addition increased. While the abrasion tests were not as consistent, they still show the same trend of a decrease in wear with increasing CrB_2. All of the samples placed in the Q-Fog showed some corrosion, particularly on the edges since they were not protected. The samples with 90 to 50 wt% chromium in the slurry had very minimal corrosion indicating that there was enough chromium present in the iron alloy to form a protective coating. Samples with less chromium (and therefore having 60 to 90 wt% CrB_2) evidenced extensive corrosion. Results from the x-ray diffraction patterns indicated the formation of additional borides, the possibility some chromium carbides (Cr_7C_3 and $Cr_{23}C_6$) as reported in previous work [6] and the absence of the initial boride CrB_2. Borides found were: CrB_4, CrB, $(Cr, Fe)_2B$ and possibly Fe_3B. Since a laser surface processed area often solidifies with preferred orientation, it was not possible to quantitatively compare the amounts of the phases. However, CrB_4 and CrB were more dominant in the samples with higher amounts of chromium while Fe_2B was more dominant in the samples with the higher amounts of added CrB_2. This indicates when chromium was more available the reactions were driven towards those compounds that are higher in chromium. In contrast, when there was minimal or no chromium alloyed with the CrB_2, then the reactions were driven towards those with less chromium and containing iron. An additional sample was processed that contained only CrB_2 in the slurry. SRD analysis on the surface revealed primarily CrB_2, substantiating the conclusion that the presence of additional chromium drives the reactions toward other chromium borides. The iron boride phases were not observed in the absence of chromium. A sample processed with only chromium in the slurry produced the Fe-Cr phase and some evidence of chromium carbides (Cr_7C_3 and $Cr_{23}C_6$). X-ray diffraction patterns taken after the wear tests showed no significant change in the phases present with the possible occurrence of some Fe_3B.

TABLE IV
Analysis and Test Results

	Speed (mm/min)	Hardness (Knoops)	Dry Wear (gms/min)	Abrasion (gms/rev)	Corrosion	Cross-Section	Layer wt %Cr	Surface wt %Cr
90Cr/10CrB2	1000	351	0.0009	2.81167E-05	Low Rust	ok	22.6	67.0
	1500	383	0.00095	2.795E-05	Low Rust	ok	20.0	66.5
80Cr/20CrB2	1000	404	0.00045	2.47E-05	Low Rust	ok	18.8	38.5
	1500	525	0.0005875	2.43333E-05	Low Rust	ok	24.3	45.5
70Cr/30CrB2	1000	509	0.000375	2.23333E-05	Low Rust	ok	27.5	43.5
	1500	634	0.0004625	2.66667E-05	Low Rust	ok	22.3	40.5
60Cr/40CrB2	1000	666	0.0002625	1.38333E-05	Low Rust	cracks	29.5	35.5
	1500	817	0.0006875	2.61667E-05	Low Rust	cracks	24.5	35.0
50Cr/50CrB2	1000	933	0.0003	2.03333E-05	Low Rust	spaces	30.8	19.0
	1500	1006	0.000225	1.05E-05	Low Rust	spaces	30.3	32.5
40Cr/60CrB2	1000	1235	0.00025	2.00333E-05	Rust	spaces & chunks	32.5	20.0
	1500	983	0.0002125	5.26667E-06	Rust	spaces & chunks	17.3	24.0
30Cr/70CrB2	1000	1558	0.0002375	7.98333E-06	Rust	spaces	30.0	17.0
	1500	1534	0.0002	3.3E-06	Rust	more spaces	25.5	31.0
20Cr/80CrB2	1000	1312	0.0001375	4.6E-06	Rust	spaces	27.7	15.0
	1500	1925	0.00015	3.31667E-06	Rust	spaces, chunks, pores	26.0	22.5
10Cr/90CrB2	1000	1385	0.0002125	5.66667E-06	High Rust	spaces	20.0	12.5
	1500	1269	0.0001375	4.06667E-06	High Rust	spaces, chunks, pores	34.0	22.0

IL-6034

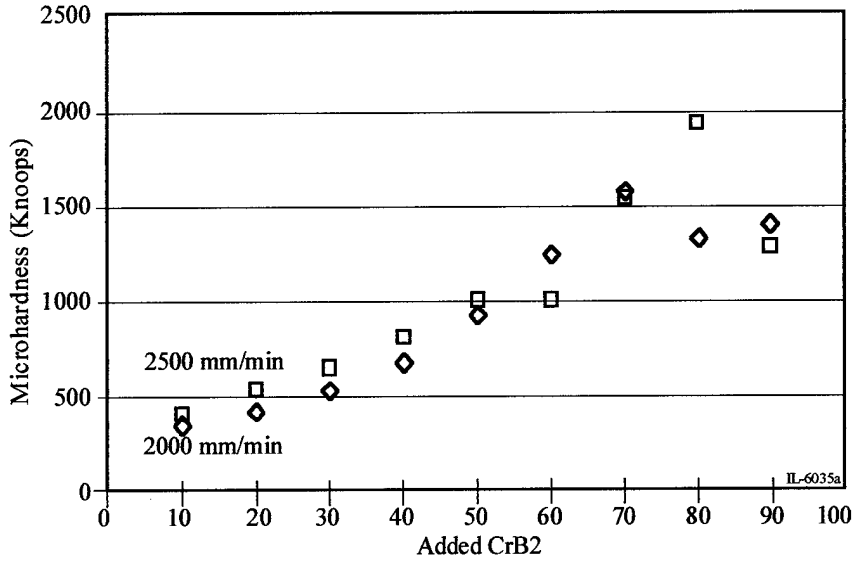

Figure 8. Microhardness as a function of the added CrB_2 for two processing speeds.

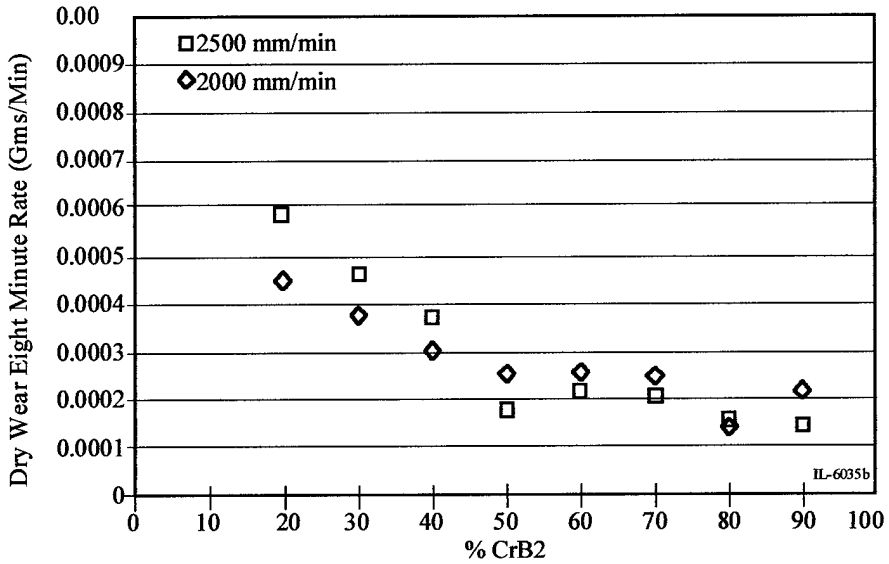

Figure 9. Dry wear rates as a function of the added CrB_2 for two laser processing speeds.

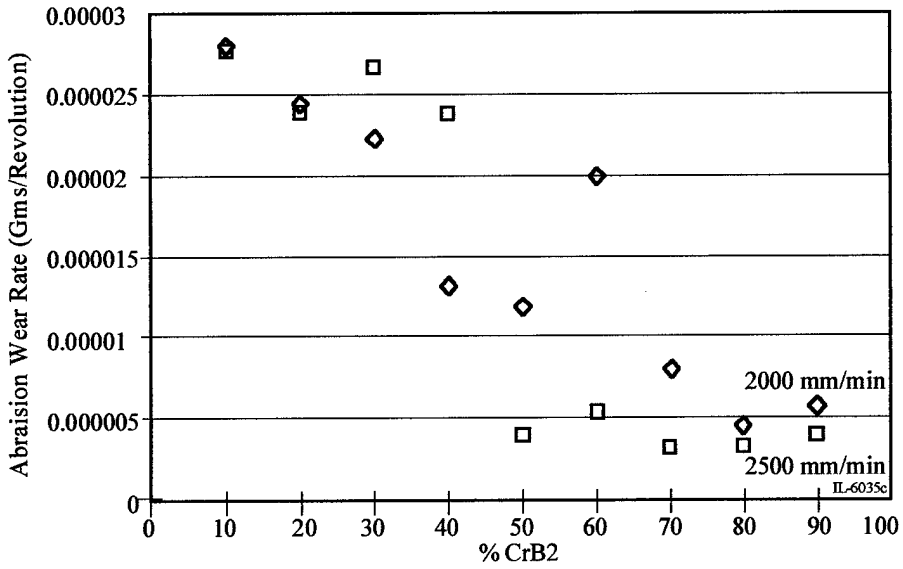

Figure 10. Abrasion wear rates as a function of the added CrB_2 for two laser processing speeds.

Figures 11 through 13 show representative microstructures from three of the samples. Figure 11 contains the most precursor chromium (90 wt%) and least CrB_2 (10 wt%). The solidification structure is uniformly dendritic with the microhardness varying by no more than ten Knoops from the surface to the interface. Figure 12 shows the structure of a sample processed with 50 wt% Cr and 50 wt% CrB_2 in the precursor. The larger white particle has a hardness of 1718 Knoops indicating that it might be a partially dissociated CrB_2 particle which should have high hardness. The rest of the matrix varies from 1000 to 2000 Knoops. The dark band at the interface has a hardness of 375 Knoops and is due to the initial solidification occurring epitaxially on the substrate. In regions where the solid particles occur, the white trunks are seen to nucleate from those particles. This is shown in a higher magnified photograph in Figure 14. Figure 13 shows a view of the sample with 20 wt% chromium and 80 wt% CrB_2 in the precursor. The boride columns are considerably more dense than in Figure 13 as is evidenced by the microhardness measurements of 1640 Knoops in those regions.

Figure 11. Microstructure of laser processed layer (1500 W 1000 mm/min) with 90% Cr/10% CrB_2 precursor addition.

Figures 12. Microstructure of laser processed layer (1500 W 1500 mm/min) with 50% Cr/50% CrB_2 precursor addition.

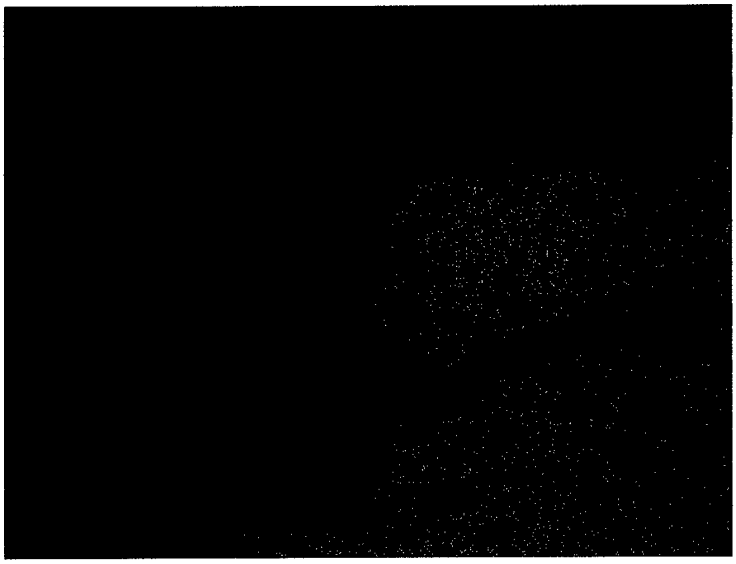

Figure 13. Microstructure of laser processed layer (1500 W 1500 mm/ min) with 20% Cr/80% CrB_2 precursor addition.

(a)

Figure 14a and b. Microstructure of laser processed layer (1500 W 1500 mm/min) with 50% Cr/50% CrB_2 precursor additions showing growth of columnar structure from large particles.

(b)

II. Solid State Transformation Regions

4340 Processing Trials

A significant focus of the effort is the delineation of mechanical properties based on processing conditions. Therefore, a sequence of experiments without slurry additions was conducted in which coupons of 6 mm thick 4340 plate were processed using a Nd:YAG laser beam with dimensions of 3 mm x 1 mm and a power of 500 Watts. As discussed earlier, 4340 steel is a high strength structural material that is heat treated to achieve desired properties. As a result, when this material is laser surface alloyed, there are considerable metallurgical phenomena that can occur beneath the molten region [7, 8]. The beam translation rate and index were the primary processing variables (see Table I). Two sets of trials, each with a different beam translation index between consecutive tracks, were completed. Variations in index yielded different amounts of overlap between the adjacent processed regions but within the beam width. The resultant surface modified regions ranged in maximum depth from 240 microns to 300 microns, with total widths up to 35 mm (or ten laser tracks). Selected track sequences on each sample were submitted to examination at 100 micron intervals, as shown in Figure 15, to produce maps of microhardness.

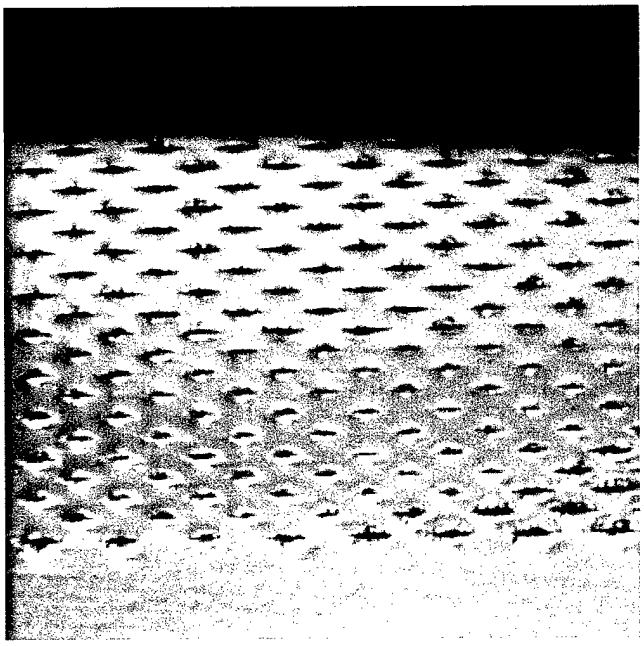

Figure 15. Illustration of microhardness indentions (100 μm spacing horizontal and vertical with 50 μm offset).

Figures 16 and 17 are microhardness contour maps for beam translation rates of 1000 mm/min and 4500 mm/min, respectively, for the beam index of 1.5 mm. Although the laser energy does not initiate melting, the microhardness results for the lower translation rate cases indicate that a transition from ferrite to austenite and then to martensite has occurred. Thus in these cases, the hardness is modified by solid-state phase transformation at locations within the sample at which the temperature reaches the austenization temperature (approximately 1000 K). The subsequent cooling rates are sufficiently high in all cases to promote the austenite-martensite transition. Note that at 4500 mm/min, the depth at which hardening occurs is not measurable.

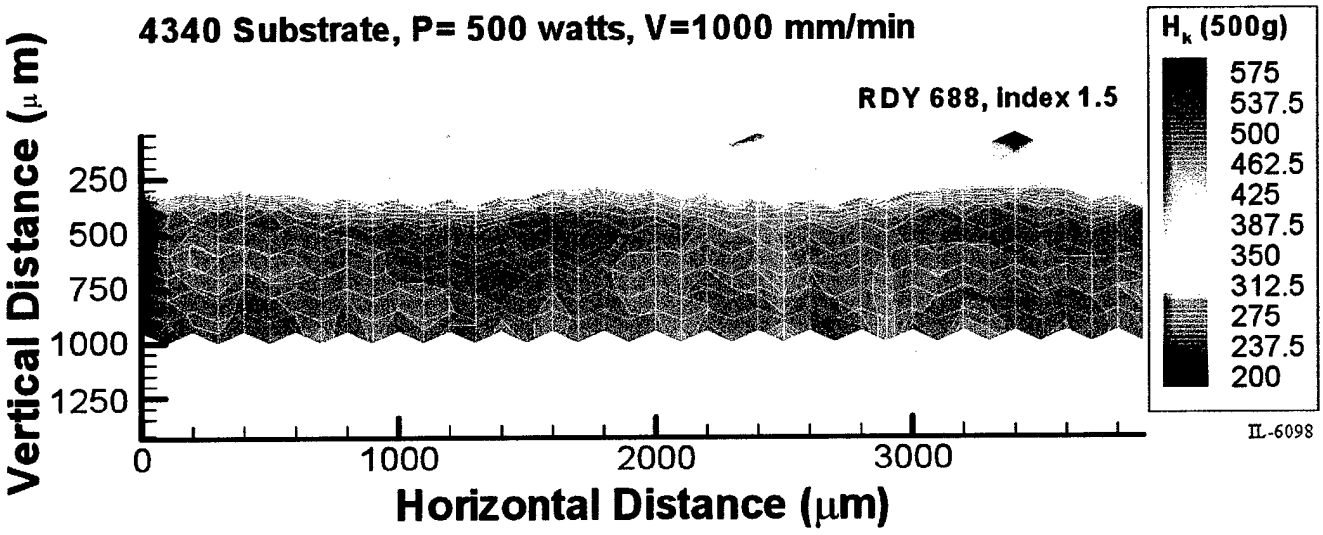

Figure 16. Microhardness contour for 1000 mm/min beam translation rate.

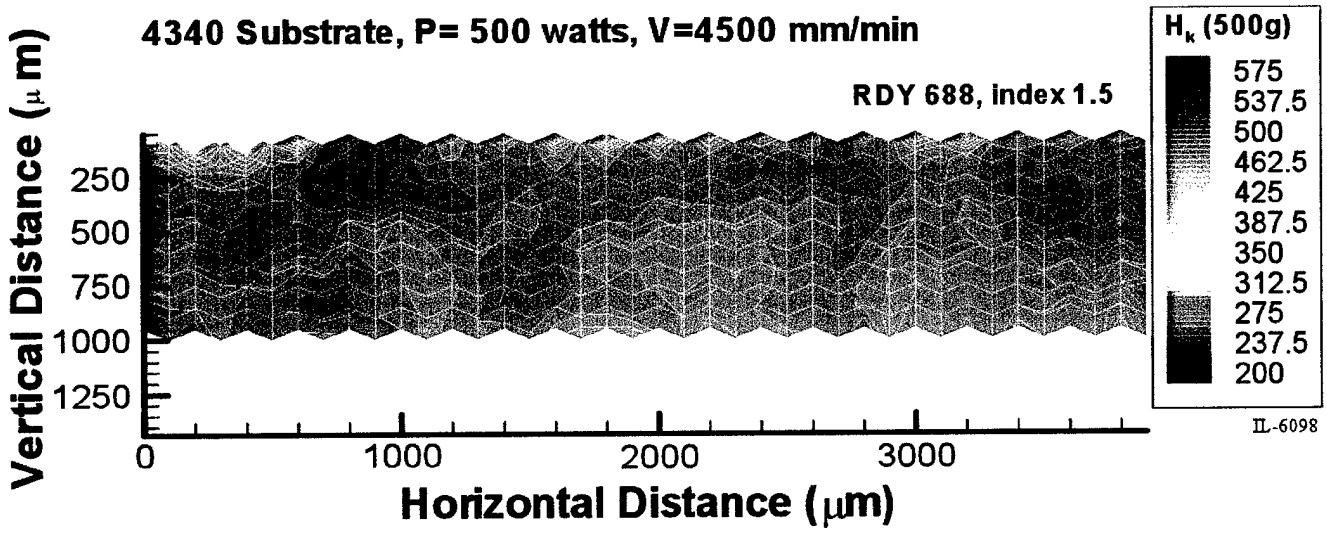

Figure 17. Microhardness contour for 4500 mm/min beam translation rate.

Figure 18 is a composite of several contour plots of measured microhardness as a function of translation rate for the beam index of 2.5 mm, illustrating that case depth increases with decreasing translation rate.

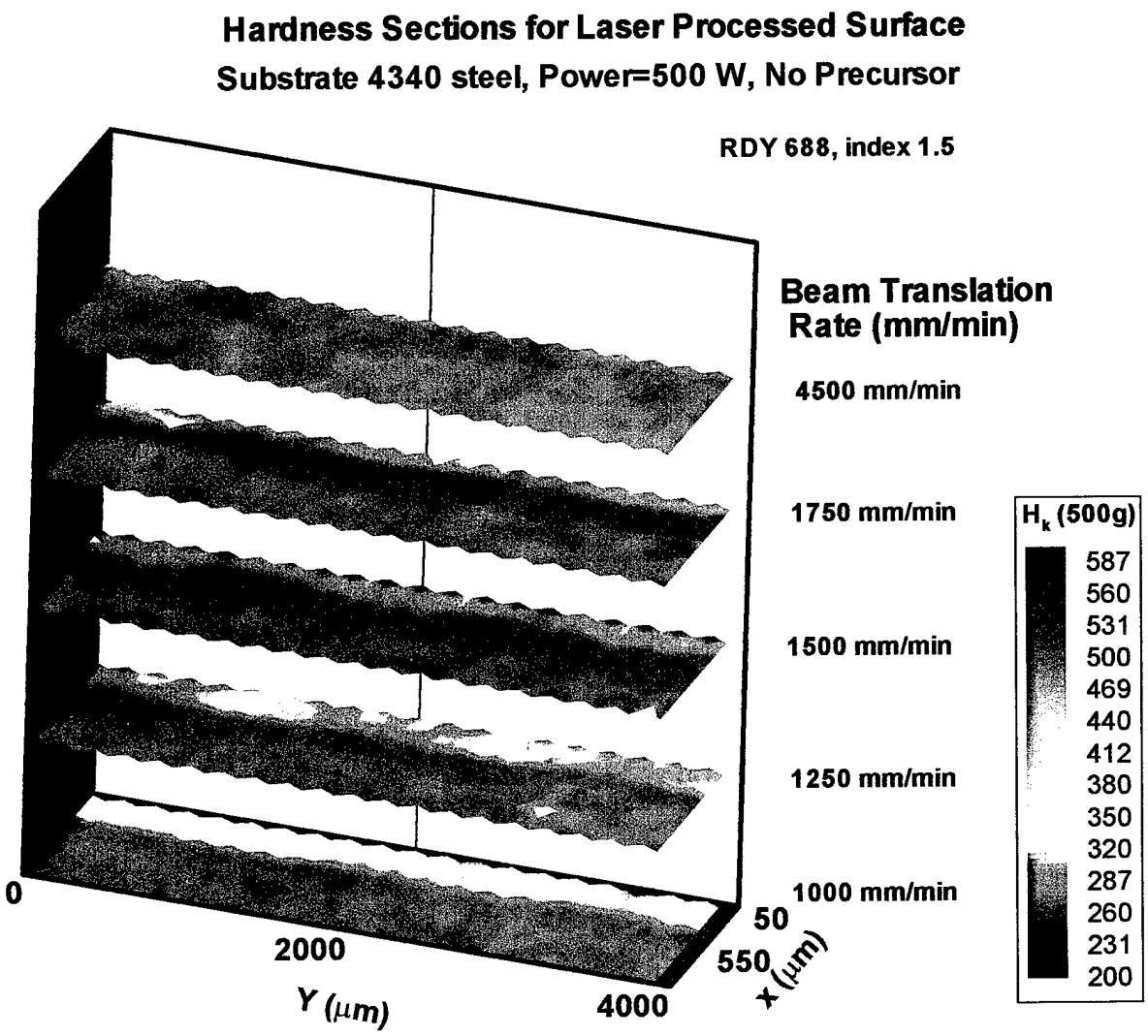

Figure 18. Microhardness map illustrating dependence on beam translation rate.

Based on the cooling rates and temperatures expected throughout the heat treated region, the presence of a uniform martensitic layer of some depth (approaching zero depth as translation velocity increases) was expected. However, the hardness measurements indicated the additional effect of a soft region near the surface even though temperature calculations based on equilibrium heating and cooling curves for the ferrite-austenite-martensite transitions predict a purely martensitic region. X-ray analysis for austenite also shows that there is no appreciable austenite in the layer. The rate of carbon diffusion in pre-austenite phases has been shown to be of importance in determining martensite hardness in cases of low heating/ cooling rate laser processing [9], and this may be the case here. However, there is also the possibility of incomplete austenitization based upon the high heating rates for the laser process and the additional effect of grain growth during the longer period of high temperature, which is experienced near the surface. This is being investigated further.

Heat Treated 4340 Processing Trials

In view of the above results, additional studies were undertaken that included heat-treated 4340 steel. Two sets of 4340 steel were prepared. One set was heat treated by bringing to 830°C and quenched in oil. The second set remained as received in the non-heat treated condition. The base hardness of the heat treated sample was 680 Knoops, and the base hardness of the non-heat treated set was 340 Knoops. A series of laser tracks were then run on each sample using the conditions in Table I. Measurements were taken of the melt zone depth, the melt zone with HAZ depth, and the melt zone, HAZ and tempered zone depths. These are shown plotted in Figure 19a and b. It can be seen that the melt zone depths are similar for both the as-received and heated treated samples and they follow a linear relationship with power/velocity. The melt zone with HAZ depths are also similar for both samples sets, but they do not have a linear relationship to power/velocity. Instead their linear relationship is to $[\text{power/velocity}]^{1/2}$. The tempering zone depth follows the same relationship as the HAZ. This implies that during laser surface alloying, a process which is generally confined to the surface and near-surface region of a material, considerations of heat flow are complicated by a transition from two-dimensional surface effects to three-dimensional effects at depth. Two parallel sets of microhardness measurements were taken through the cross-section of each track at 50 micron increments with an automated microhardness tester. Typical results are shown in Figure 20a and b, for a power of 1500 watts at three speeds.

The heat-affected zones are obvious in all of the samples, however, there are several differences in the two sets of plots: (1) the HAZ in the as-received samples are relatively flat whereas the HAZ in the heat-treated samples have distinct slope; (2) The heat-treated samples display a tempered region immediately below the HAZ while the as-received samples do not. The change in slope of the HAZ in the heat-treated samples represents an additional phenomena which occurs when a steel such as 4340 is reprocessed (e.g., essentially laser heat treated over an area that has been previously heat treated and quenched). The region near the surface has experienced two temperature cycles that reached above the austenite transformation temperature and dropped rapidly to produce martensite. The microhardness plots in Fig. 20a and b show the effects of a second cycle. The reduction in hardness towards the

surface after the second cycle is thought to be due to either grain growth or a depletion in carbon since the longer times at temperature encourage diffusion.

One aim of this segment was to combine temperature and time predictions with the microhardness data to establish a rate law that could be used in predicting the reaction rates in these regions, and therefore properties for a given set of conditions. Since transformation mechanisms taking place, particularly in the tempered region are not well understood, it was not possible to develop a theoretical set of formulations, therefore an empirical approach was adopted.

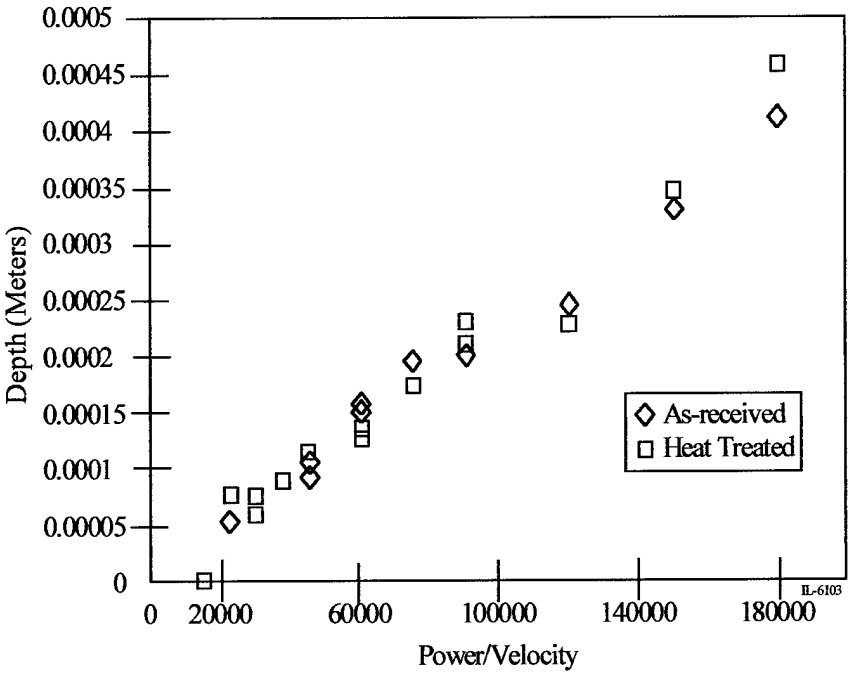

Figure 19a. Melt zone depth as a function of power/velocity for the as-received and heat-treated samples.

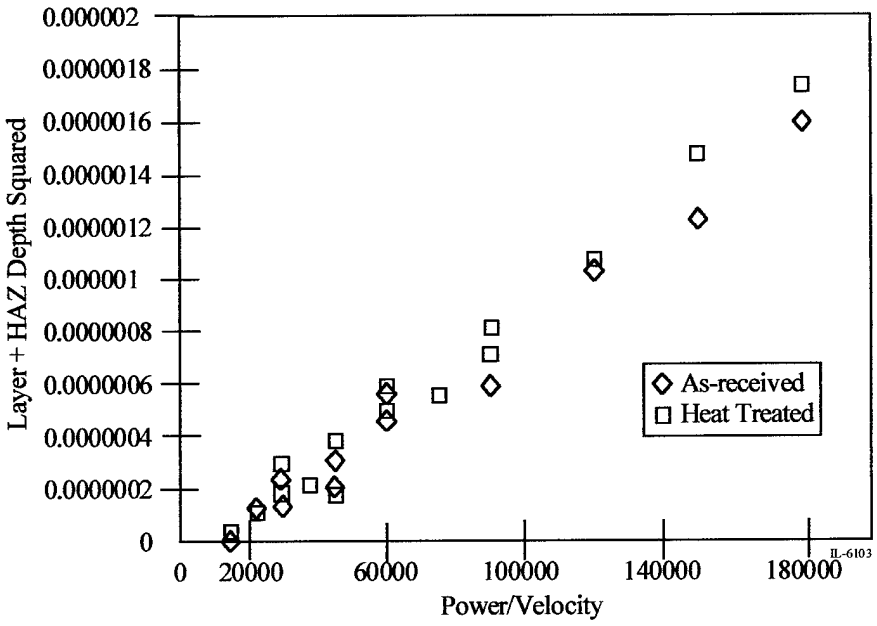

Figure 19b. The square of melt zone with HAZ depth as a function of power/velocity for the as-received and heat-treated samples.

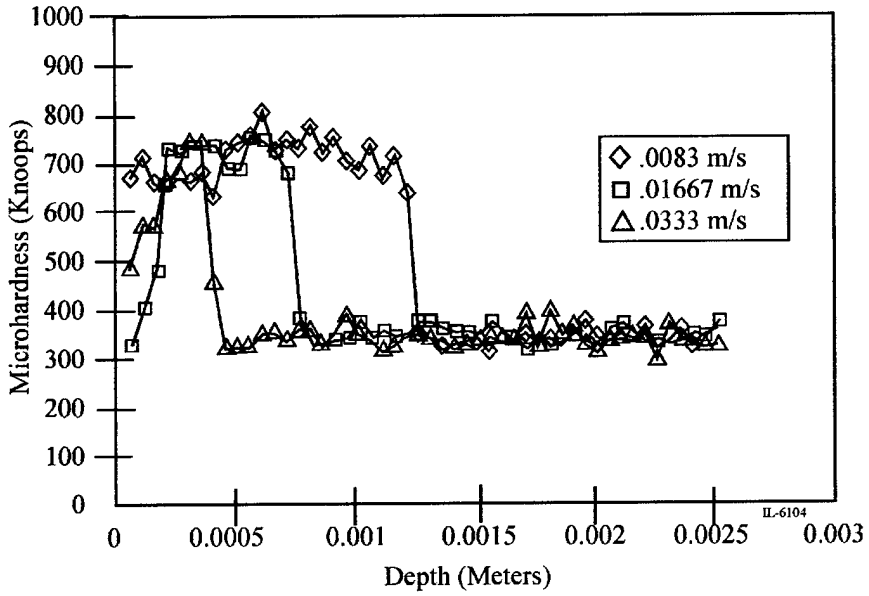

Figure 20a. Microhardness measurements of as-received samples processed at 1500 watts and three speeds.

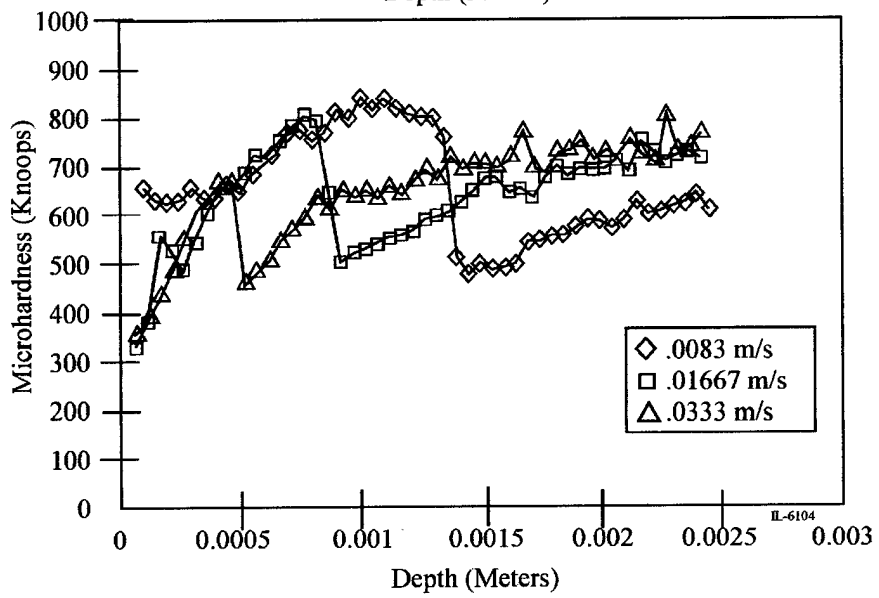

Figure 20b. Microhardness measurements of heat treated samples processed at 1500 watts and three speeds.

Since tempering has a time-temperature relationship, these parameters can be related through a rate equation such as,

$$1/t = A \exp(-Q/RT)$$

where t is time, A is a dimensionless constant, R is the gas constant, Q is an activation energy representing the process, and T is temperature. The effectiveness of tempering is often expressed in terms of hardness and so this equation can be rewritten as [8]

$$\text{Hardness} = f[tA \exp(-Q/RT)]$$

The simplicity of this equation is dependent upon certain assumptions such as: A, which reflects the microstructure is independent of temperature and Q is independent of hardness. Hence, the activation energy Q for a reaction can be obtained from data that is gathered as a function of temperature. Some typical activation energies of interest are given in Table V.

TABLE V

REACTION	ACTIVATION ENERGY (CAL/MOLE)
Carbon diffusion in fcc iron	34,000
Carbon diffusion in bcc iron	29,300
Iron diffusion in fcc iron	64,000
Iron diffusion in bcc iron	57,500
Cementite growth at 300°C	48,500-j/mole IL-6096

The larger the activation energy, the slower the reaction.
Measurement of the activation energy Q in the tempered region was undertaken using the sets of microhardness data for the two base materials. In order to represent the time-temperature relationship, the depths of the molten zone and HAZ were fit to an existing empirical equation [9]. Using these corrections on the model material parameters, the time period over which each microhardness mark location was at an elevated temperature was calculated. The inverse of this time was then plotted logarithmically versus the change in microhardness with time at selected peak temperatures. Figure 21 shows this plot. An activation energy of 35 kcal/mol can then be obtained from Figure 21. This is in line with the diffusion of carbon in iron, and although it is based on an analytical calculations gives an indication of the controlling phenomena. It also indicates the value and the need for an accurate computational model that is validated by experimental data. Such an effort was undertaken in the third phase of this project.

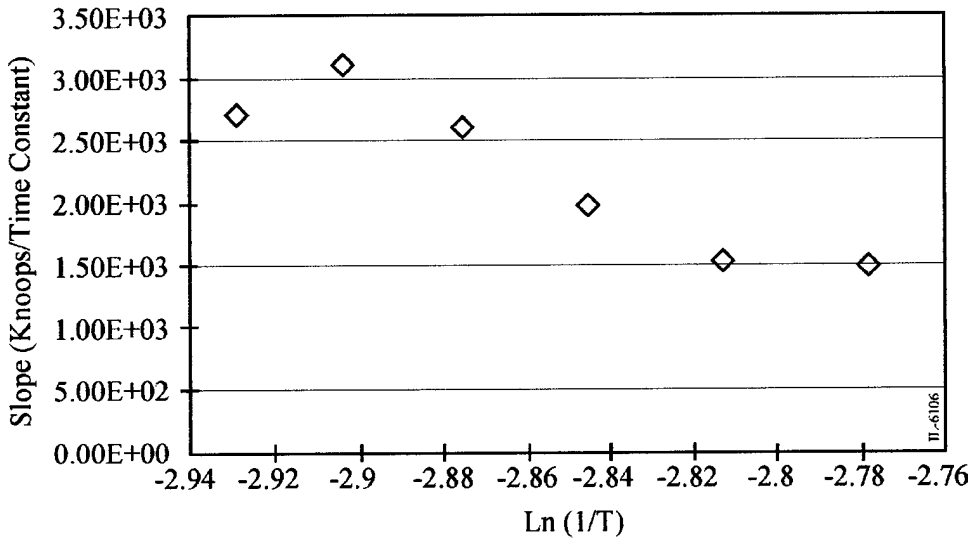

Figure 21. The slope of hardness/time as a function of the ln(1/T) where T is temperature.

III. Experimental and Computational Thermal Studies

Thermocouple measurements were used to determine the heating and cooling rates during laser surface processing. Because mechanical measurements were being made on a micro-scale, and regions of interest may span only 150 microns, temperature measurements on the same scale were desired. One basic objective of the measurements was to determine directly the thermal cycle in the near melt region. In order to accomplish this, thermocouples must be placed in this region in such a way that they represent the actual temperature in this region. This was accomplished for the short span of time before the thermocouple reaches its melting temperature. Figure 22 is a comparison of temperature measurements made at the same sample location for trials of differing index. The temperatures for the small index case are noticeably higher than the large index case. In some cases the temperature may be sufficient to provide an annealing process for previously processed material. This has been observed in some samples with very small beam index (.25 mm).

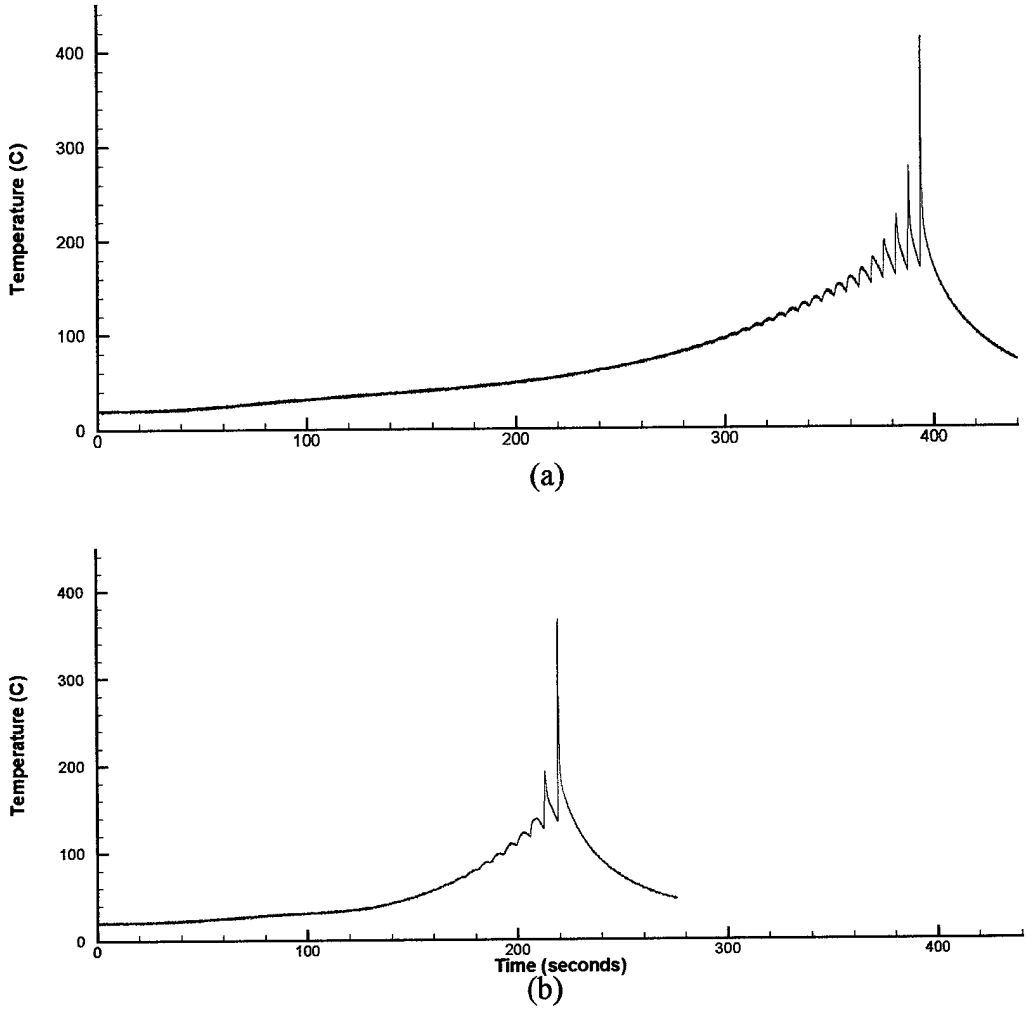

Figure 22. Comparison of thermocouple measurements for 3 mm and 2 mm beam index values. (a) small index case, and (b) large index case.

Several computational models were developed for predicting the three-dimensional, time-dependent temperature in the processed samples and were used to investigate the influence of various operating conditions on the process. One was a finite volume model that can accurately predict multi-species convective transport, and the other was a finite element model that can be used to predict thermally induced stresses. Although there was some overlap between the models, they provided different physical information, and the objective was to calculate the temperature and species transport with the finite volume model, and use this as input to the finite element stress model.

The ultimate goal of the model development was to determine the most important characteristics of the laser surface processing; melt pool dimensions and chemical composition distribution being two primary examples. However, the importance of the time dependence of temperature in determining solid phase formation drove the initial efforts at modeling the process towards solving the simple three-dimensional heat equation, i.e., the time dependent diffusion equation. While the actual temperature field can be determined only by solving the full set of coupled conservation laws and accurately assessing the physics of the phase transformation at any phase transition boundaries, the heat conduction equation is useful as a first approximation to the temperature field in the sample.

The thermal model is an aid in predicting cooling rates for a material that has been laser processed. Since there are several process variables that must be considered (beam power, beam speed, overlap index), a model can be used to determine cooling rates for a given set of conditions. In any given track, in addition to the phase transformations within the melt pool, there can be significant heating in the heat affected zone (HAZ), i.e., the regions adjacent to the melt pool that are heated to temperatures close to, but below the melting point. Since there is a solid state phase transition at 1000 K in steel and melting typically occurs around 1700 K, it is of interest to know which regions in the vicinity of the melt pool are heated above the transition temperature. The model can determine this region. The model can also be used to determine the cooling rates of the HAZ, in order to estimate the phase distribution around the melt pool.

Since the surface processing utilizes a cyclic process, there are multiple beam tracks offset by a given index, and it is possible that the HAZ of one track may overlap the melt pool of a prior track and yield an additional solid state phase formation. It is important to determine if, for a given set of conditions, there is enough overlap to heat processed regions to temperatures above the lower transition temperature, and hence possibly transforming it into a different phase than that immediately following the original transition from liquid to solid.

For the finite volume model, the commercial computational fluid dynamics code, CFDACE+ (CFD Research Corporation, Huntsville, AL), was used to solve the energy equation. The model is run on a PC using the Windows NT (v4.0) operating system. CFDACE has the advantage that, in the future when momentum and mass transport will be included, it can solve the coupled equations associated with fluid flow, and hence can be used to model the mixing and distribution of species within the melt pool. In the current model there is no consideration of mass, momentum, or species transport.

Figure 23 depicts the domain of the problem. The size of the 3D computational domain is limited by memory. The scale of the laser requires a fine grid in the vicinity of the beam in order to model the beam profile and steep thermal gradients around the beam. Because the model is memory limited, each computational grid is tailored to a specific set of processing conditions. The grid in Figure 23, for example, is designed to handle three tracks with an overlap index that is 1/2 the width of the beam. If the five densely packed regions in the center of the grid are hypothetically numbered 1 through 5 in order, then the first track would be centered on 2 with the edges of the beam located in 1 and 3. The second track would similarly be centered on 3, with the beam edges located in 2 and 4. Other processing parameters are used to define other unique grids.

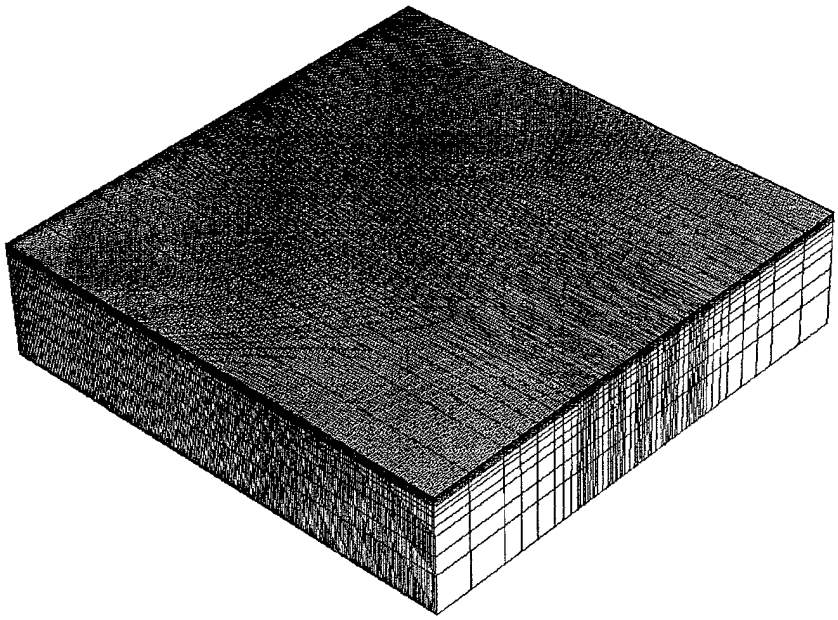

Figure 23. Computational Grid (251 points in the direction of the beam movement, 16 points vertical, and 62 points perpendicular to beam movement).

The grid spacing is varied in both the y direction and z direction in order to pack points near the beam. The *x* direction cell spacing is 100 μm. the *y* direction cell spacing varies from 2000 μm at the edge of the model to a minimum of 150 μm in the densely packed "track" regions. The *z* direction cell spacing varies from 2000 μm on the side away from the beam (adjacent to the heat sink) to 30 μm at the processing surface. Memory constraints limit the model to a volume of 2.5 cm (*x*, I = 251) x 2.5 cm (*y*, J = 62) x 6 mm (*z*, K = 16).

The boundary conditions are selected to closely approximate actual processing conditions, i.e., convective/radiative and or fixed temperature. Since a shield gas is typically used, the convective heat transfer coefficient is somewhat higher than "natural," 30 W/m^2 K, to account for the forced flow of gas around the sample. All five exposed sides use this value. The sample is mounted to a water-cooled heat sink, so the bottom side could be set to a fixed temperature. However, experience shows that the water flow can only remove some of the energy building into the heat sink, and thus an alternative boundary condition, is to use convection (no radiation) with a high (500 W/m^2K) heat transfer coefficient.

Two beam profiles that were modeled; an elliptic Guassian and rectangular tophat, both with a possible temperature dependent absorption coefficient.

The Guassian beam is of the form:

$$q_b(x,y,t) = \alpha I_o \exp\left[-\left(\frac{x-x_o(t)}{x_r}\right)^2 - \left(\frac{y-y_o(t)}{y_r}\right)^2\right]$$

while the rectangular tophat is of the form:

$$qb\,(x, y, t) = \alpha I_0 \quad \text{when} \quad |x - x_0\,(t) \le x_r \text{ and } |y - y_0\,(t)| \le y_r$$
$$= 0 \quad \text{otherwise}$$

where $x_0(t)$ and $y_0(t)$ are the coordinates of the center of the moving beam. For the Guassian beam profile, x_r and y_r are the beam radii to the 1/e point in their respective directions for the rectangular tophat profile, x_r is 1/2 the beam width in the x direction and y_r is 1/2 the beam width in the y direction.

I_0 is the beam intensity at the center of the beam and can be found from the beam power, P, using

$$I_0 = \frac{P}{c x_r y_r}$$

where c is π (3.14159) for the Guassian profile and 4 for the rectangular tophat profile.

Solving the time dependent heat equation requires only the density, thermal conductivity, and specific heat. The density is assumed constant, while the conductivity and specific heat are functions of temperature. Additionally, since the model does not incorporate phase changes explicitly, the latent heats of formation are included in the specific heat. Figure 24 illustrates the enthalpy distribution for the shown temperature profile using the specific heat of Table VI.

Figure 25 shows the isotherms of the temperature field at various times during processing with a low power (200 W) beam. Note that even in this case of minimal energy input, there is evident preheating of the sample for subsequent laser tracks. This yields an increasing maximum temperature, and, together with the thermal boundary conditions, an asymmetry in the temperature distribution.

Figure 26 compares the measured temperature profile during processing using a moderate power (500 W) beam with modeled values using a rectangular tophat beam profile with the same power. Calculated heating and cooling rates match measured values very well. Slight differences can be attributed to measurement technique.

In addition to the volume control model, a finite element model was constructed using the software package COSMOS/M. The objective for this model is to predict (or input from the CV model) the temperature field and resulting stresses during and after LISI processing.

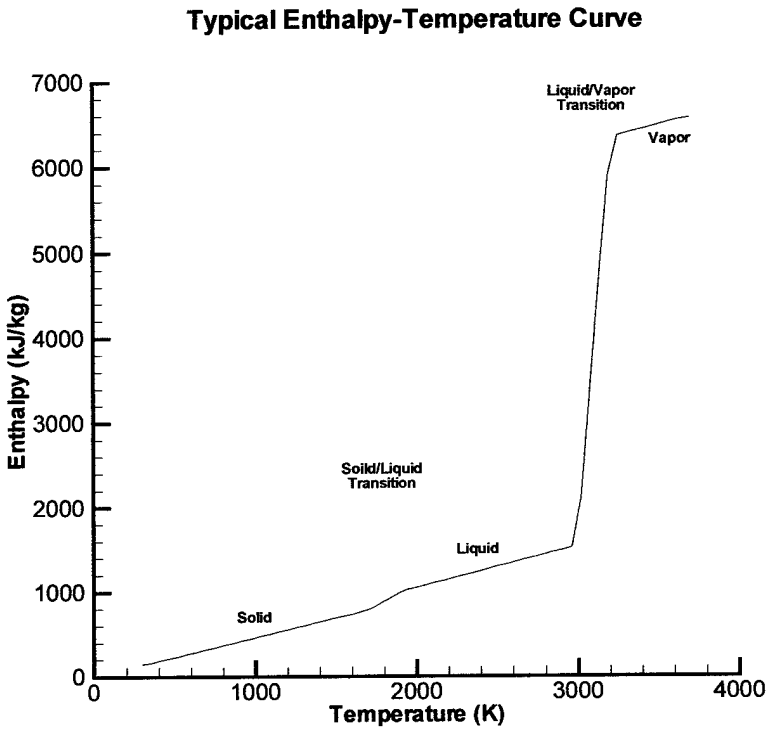

Figure 24. Enthalpy as a function of temperature.

TABLE VI

Typical Specific Profile for a "Steel"

Temperature Range (K)	Specific Heat (J/kg K)
1-1700	460
1700-1900	1100
1900-3000	490
3000-3200	24000
3200-	500

IL-6096

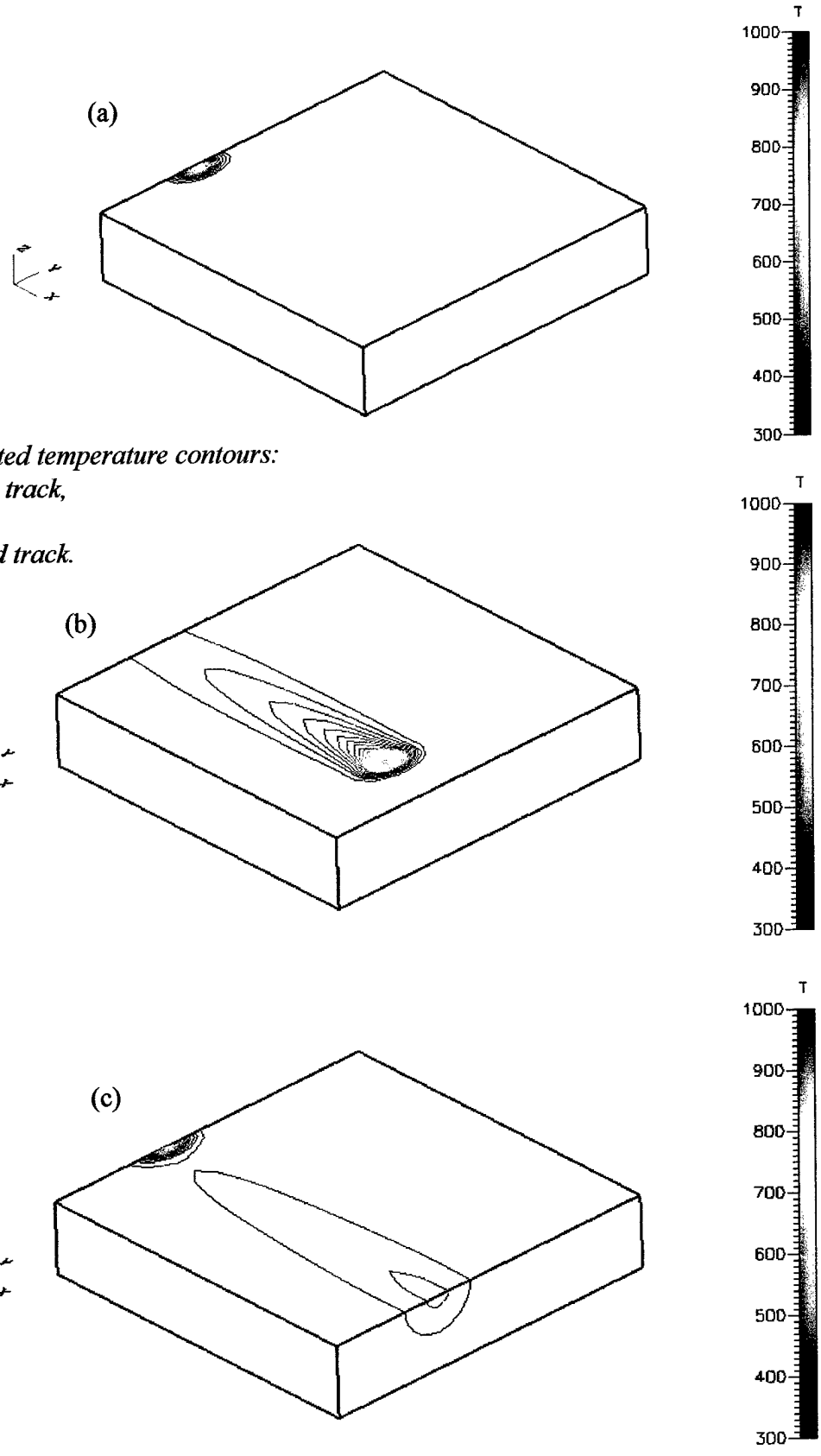

Figure 25. Calculated temperature contours:
(a) beginning of 1st track,
(b) end of 1st track,
(c) beginning of 2nd track.

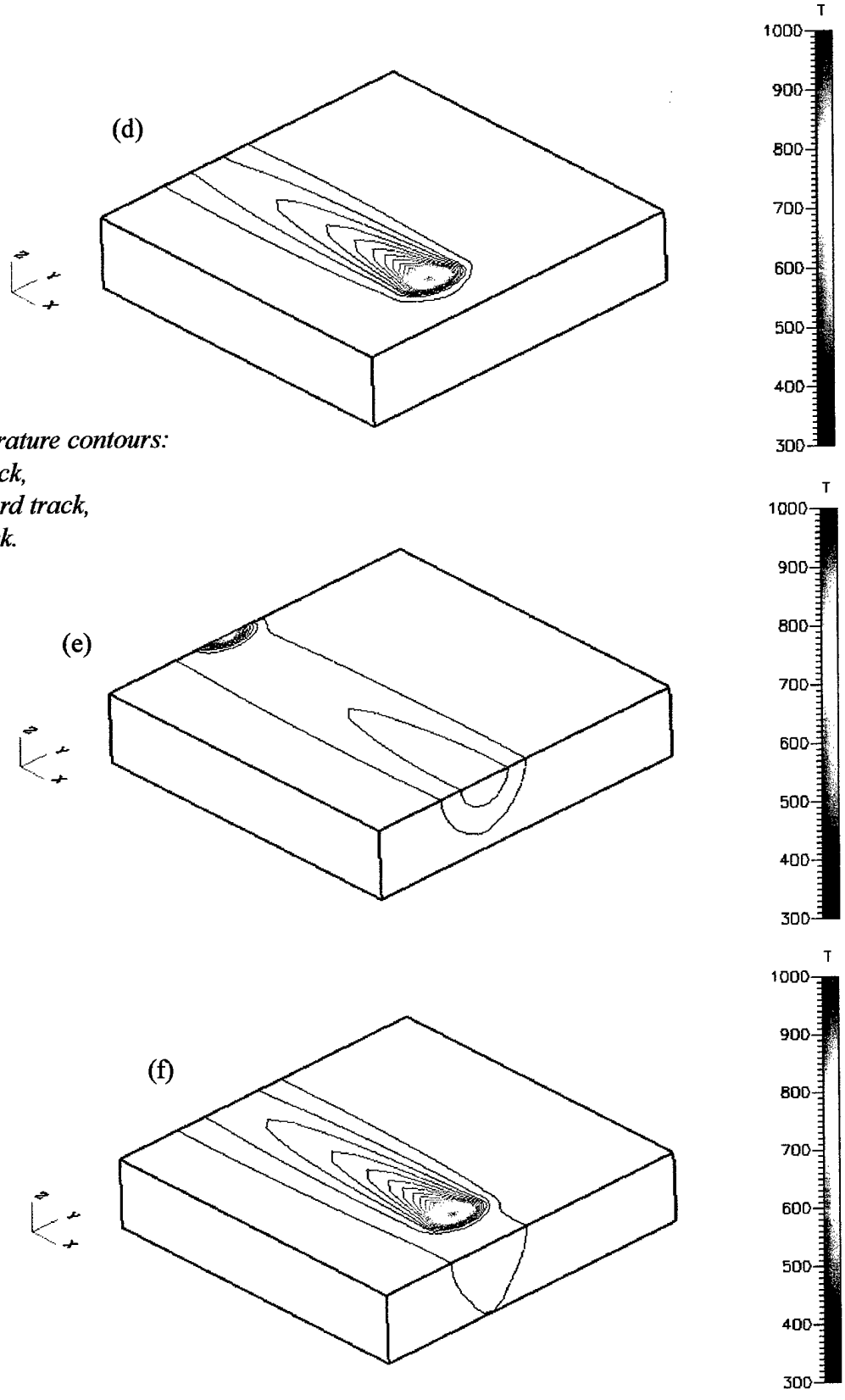

Figure 25. Cont.
Calculated temperature contours:
(d) end of 2nd track,
(e) beginning of 3rd track,
(f) end of 3rd track.

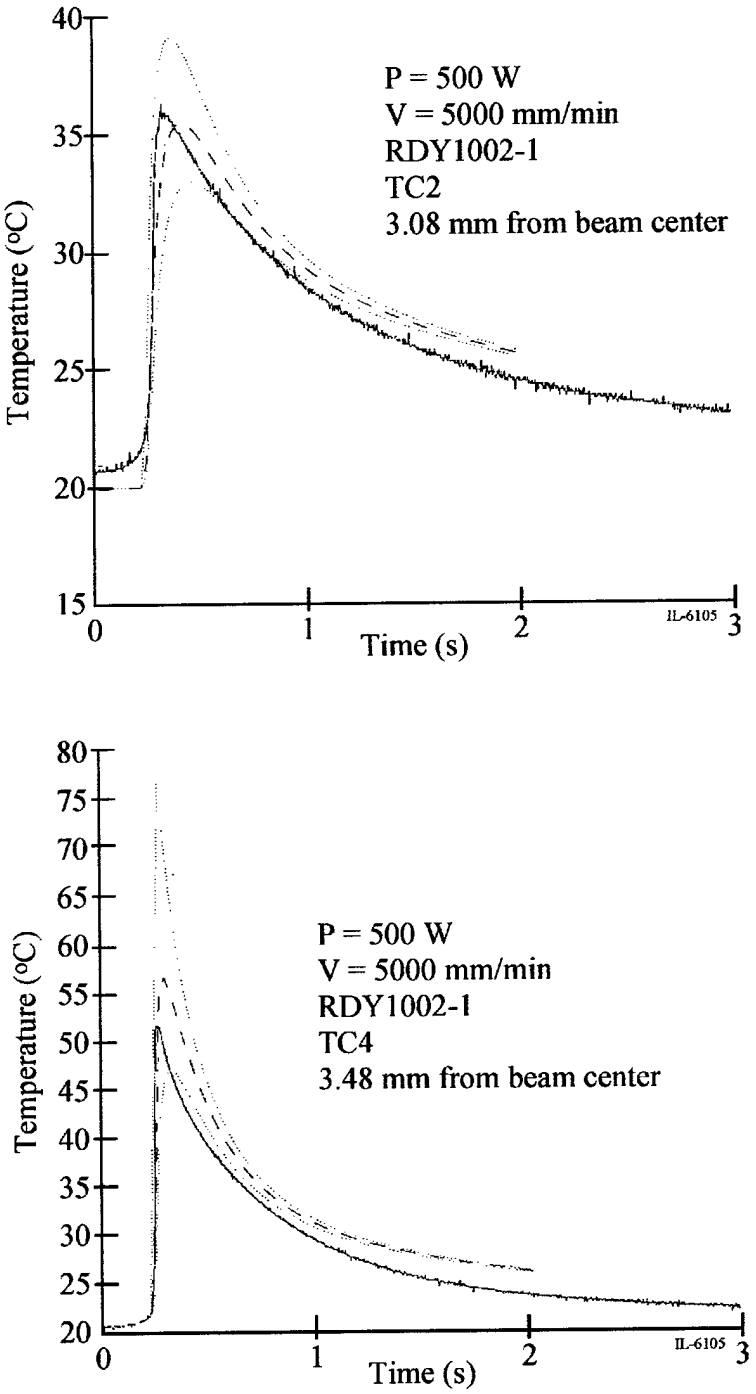

Figure 26. Comparison between modeled and measured time dependent surface temperatures at two different locations. The solid lines represent thermocouple measurements. The dashed lines represent modeled temperatures at the same location. The dotted lines represent modeled values 300 microns (the diameter of the thermocouple bead) closer to and further from the beam.

The problem to be modeled was similar to the sample coupons used in the processing trials, with dimensions 3 cm x 3 cm x 0.6 cm. The grid in the vertical dimension is comprised of 10 elements that have nonuniform spacing varying from .29 microns at the top surface to 1764 microns at the lower surface. There are 50 elements in each of the other directions. Boundary conditions at the side and upper surfaces are a combination of convection, h = 30 W/m^2 K (ambient temperature = 20°C) and radiation. The bottom surface is adjacent to a water cooled heat sink and is modeled by h = 500 W/m^2 K and temperature = 20°C. The distribution of energy in the laser beam is modeled as an elliptic Gaussian and the surface has an absorption coefficient of 0.54. Figure 27 shows a comparison of temperature responses at various locations at the top of the surface. Note that although the track-to-track temperature rise is evident, this model does not capture the high heating and cooling rates correctly. There is an oscillatory behavior that is especially noticeable during the initial heating of the point nearest the beam. This is a common problem with explicit time solutions, and is one reason the more robust CFD-ACE model with a fully implicit solver was selected for primary use in this project.

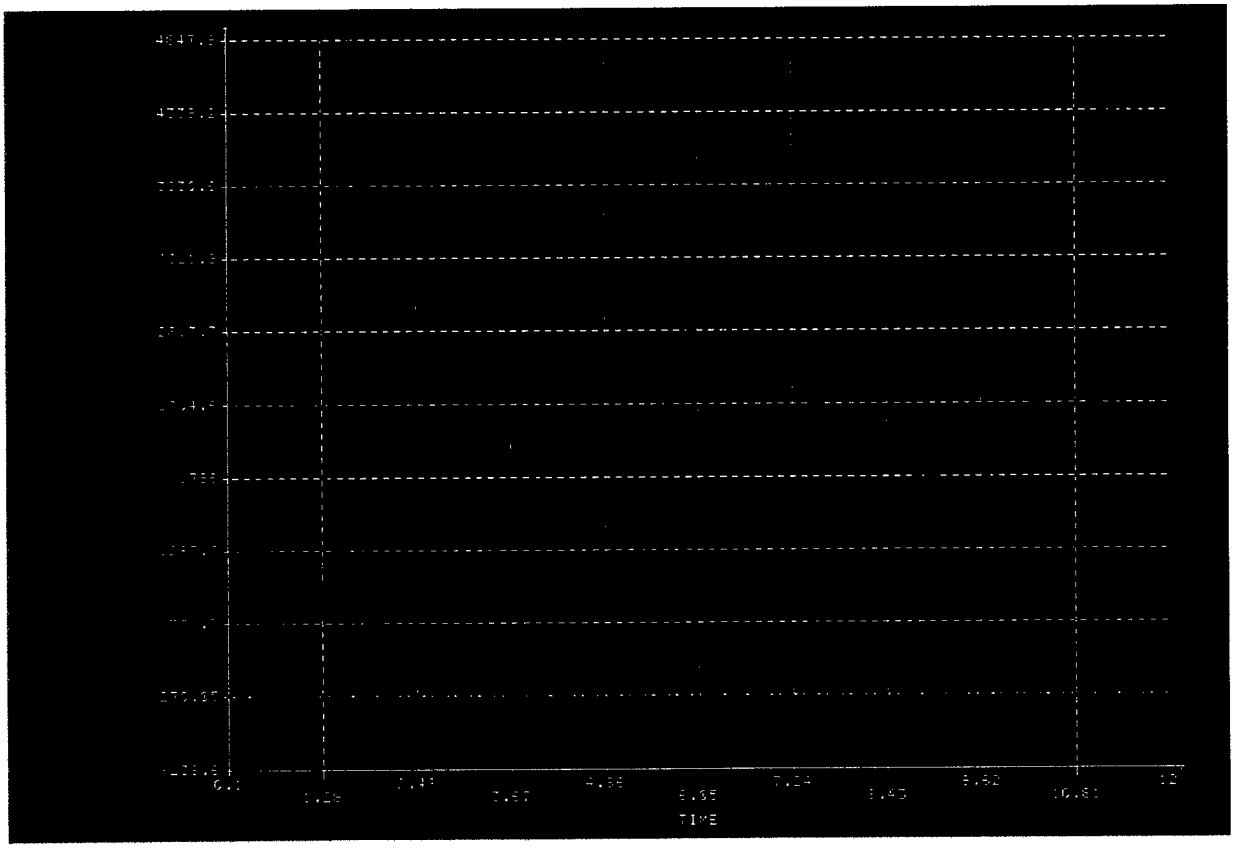

Figure 27. Calculated Temperature Response.

Figure 28 shows the calculated temperature response at the top three grid points during multi-track processing. Note that at this translation rate, all of the points shown are heated above the austenitization temperature. Thus the material at these locations will be transformed to martensite and will exhibit higher hardness than the substrate. This data can be examined to identify a hardening depth that can be compared to measurements.

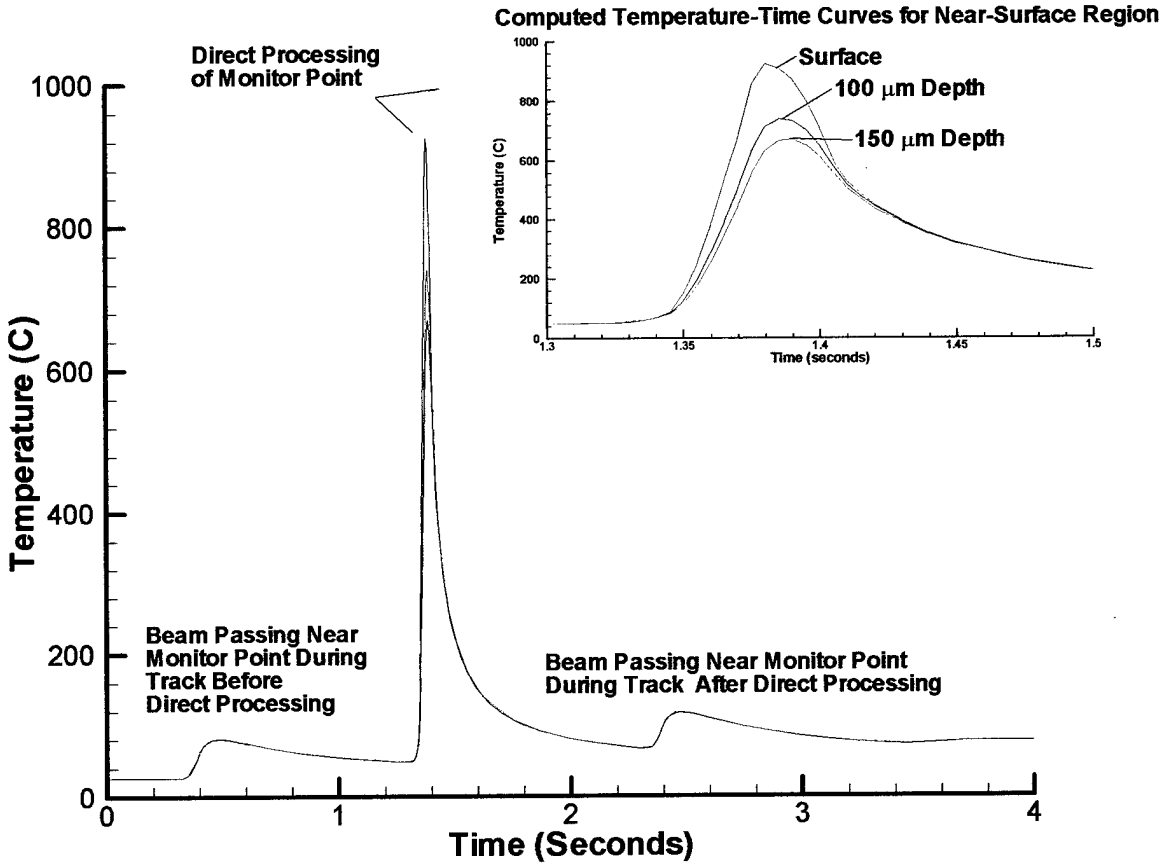

Figure 28. Temperature response at the top of the processed surface during multi-track processing.

SUMMARY

In studying laser surface alloying, there are two significant areas of concern: the alloyed surface, and the base material. The alloying process itself presents myriad potential phenomena depending upon the elements and compounds used and their affinity for chemically reacting with the base material or each other. The base material or region below the surface alloy, presents another set of interesting phenomena in that it can experience numerous metallurgical events such as martensitic transformation, tempering, grain growth, carbide growth etc. The most desirable approach to identifying the total resultant properties of such a laser surface alloyed material would be to exercise a computational model. This study attempted to begin the development of such a model while performing concurrent experiments to identify the significant chemical reactions and metallurgical phenomena that must be considered.

A systematic approach was adopted to investigating the addition of materials into the material surface. When considering steel, it was determined that the effects of elemental additions such as nickel and chromium can be predicted using existing phase information for the stainless steels. However, when compounds are included in the additive, chemical reactions occur that create important deviations from the alloy composition. These must be considered individually since the reactions are dependant both upon the relative amount of the additive and the particular additive itself. A good example from this study is the result of adding WC to steel. Decomposition of the WC into other compounds of tungsten and the addition of carbon to the matrix, produces a unique set of properties within the surface material. Although the properties such as hardness and wear resistance are improved by the WC addition, the microstructural path to obtaining those properties must still be understood and predictable.

In steels in particular, the region below the alloyed surface displays a variety of mechanical properties which depend upon the processing parameters. The energy input from the laser determines the time and temperatures which are experienced by the steel and therefore influences the solid state transformations. Although it has been thought that the speed of the laser mitigates many of these transformations, this is not the case. The transformation to austenite and then to martensite occurs within the subsecond time frame of the laser pass, and more interestingly, the region beneath the heat affected zone also has sufficient time to temper. These are effects which have been found as a result of this investigation and bear further study to distinguish between the influence of the temporal cycle on grain growth, carbon diffusion, carbide formation, and phase transformation. Processing parameters that can both produce a layer with selected properties while at the same time encouraging beneficial phase transformations below the layer exist, but within a narrow window and one that needs to be clearly examined and identified.

Utilization of a computational model for the prediction of layer and sub-layer phases is a far more desirable approach than running a multitude of laboratory experiments. However, as the experimental studies elucidated, the reactions and transformations which occur during and subsequent to processing are complicated and varied. This study began attacking that

large problem with a 3D model that could produce the melt pool and the cooling rates. Since the surface processing itself is cyclic, the indexing of the tracks was also considered since one track overlaps the solidification region and HAZ of the adjacent track. The grid spacing was varied in two directions in order to correctly model the intensity of the small beam. Calculated temperature contours for repetitive tracks were found to closely match data taken from high speed temperature measurements. Therefore the regions which exceeded both the liquid and solid transformation temperatures was identified for an actual experimental sample configuration. The influence of a previous laser track upon the subsequent track, was also distinguished. This is a significant first step in understanding and predicting the final properties of a laser surface alloyed material.

REFERENCES

1. A. L. Schaeffler, Metal Progess 56 (1949) 680, 680-B.
2. A. Solina, M. D. Sanctis, L. Paganini, A. Blarasen, and S. Quaranta, *J. Heat Treat.*, Vol. 3 (3), 1984, pp. 193-204.
3. F. F. Vaughn, V. R. Farlow, and E. R. Mayer, *Trans. ASM*, Vol. 30, 1942, pp. 516-540.
4. G. D. Rieck, *Tungsten and Its Compounds*, (Pergamon Press, New York, 1967) p. 80.
5. B. Bhushan and B. K. Gupta, *Handbook of Tribology, Materials Coating and Surface Treatment*, (eds.) (McGraw-Hill, Inc.) p. 453.
6. G. Shafirstien, M. Bamberger, M. Langohr, and F. Maisenhalder, *Surface and Coatings Technology*, 45 (1991) 417-423.
7. H. J. Hegge, H. DeBeurs, J. Noordhuis, and J. Th. M. DeHosson, *Met. Trans. A*, Vol. 21A, April 1990, pp. 987-995.
8. W.C. Leslie, *The Physical Metallurgy of Steels,* McGraw.
9. M.F. Ashby and K.E. Easterling, *Acta Metall.* (1984) Vol. 332, pp. 1935-48.